J. Fluid Mech. (2021), *vol*. 919, A41, doi:10.1017/jfm.2021.399

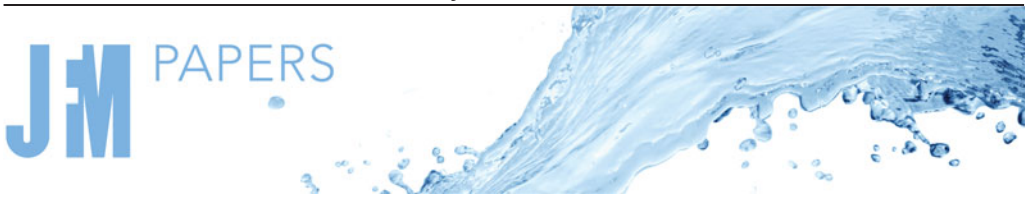

Self-similarity of turbulent jet flows with internal and external intermittency

M. Gauding[1,†], M. Bode[2], Y. Brahami[1], É. Varea[1] and L. Danaila[1,3]

[1]CORIA – CNRS UMR 6614, 76801 Saint Etienne du Rouvray, France

[2]Institute for Combustion Technology, RWTH Aachen University, Aachen, Germany

[3]Normandie University, UNIROUEN, UNICAEN, CNRS, M2C, 76000 Rouen, France

(Received 4 November 2020; revised 19 March 2021; accepted 29 April 2021)

The combined effect of internal and external intermittency on the statistical properties of small-scale turbulence is investigated in temporally evolving, planar turbulent jet flows at different Reynolds numbers using highly resolved direct numerical simulations. In turbulent jet flows, the phenomenon of external intermittency originates from a sharp layer, known as the turbulent/non-turbulent interface, that separates the turbulent core from the surrounding irrotational fluid. First, it is shown that low-order and higher-order structure functions in both the core and the shear layer of the jet satisfy complete self-preservation, which means that structure functions are invariant with time and collapse over the entire range of scales, regardless of the set of length and velocity scales used for normalization. Next, the impact of external intermittency on small-scale turbulence is studied along the cross-wise direction by the self-similarity of structure functions. It is shown that structure functions exhibit from the centre toward the edge of the flow a growing departure from self-similarity and the prediction of classical scaling theories. By analysing statistics conditioned on the turbulent portion of the jet, it is demonstrated that this departure is primarily due to external intermittency and the associated similarity-breaking effect.

Key words: intermittency, jets, turbulence simulation

1. Introduction

Fully developed fluid turbulence is characterized by strong spatio-temporal fluctuations over a wide range of different scales. Specific predictions of the statistical structure of turbulence have been provided by Kolmogorov's similarity theory (Kolmogorov 1941*a*,*b*). Under the condition of sufficiently large Reynolds numbers, Kolmogorov hypothesized that the small-scale motion decouples from the large scales and is independent of the boundary or initial conditions of the flow. The central element of Kolmogorov's scaling

† Email address for correspondence: michael@gauding.de

© The Author(s), 2021. Published by Cambridge University Press

https://doi.org/10.1017/jfm.2021.399 Published online by Cambridge University Press

theory is the velocity increment

$$\Delta u_i = u_i(\boldsymbol{x} + \boldsymbol{r}, t) - u_i(\boldsymbol{x}, t), \tag{1.1}$$

which describes velocity fluctuations between two points separated by the vector $\boldsymbol{r}$. The statistical moments of the velocity increments are known as structure functions. Kolmogorov (1941*b*) postulated that the entire distribution function of Δu_i depends for small scales only on the kinematic viscosity ν and the mean energy dissipation rate $\langle\varepsilon\rangle$. Based on a universality hypothesis, Kolmogorov derived two independent solutions for structure functions in the dissipative and the inertial ranges (Kolmogorov 1941*a*). Kolmogorov's scaling theory from 1941 is henceforth referred to as K41.

While Kolmogorov's K41 scaling theory has been confirmed to be generally valid for low-order statistics of many turbulent flows, there are numerous experimental and numerical studies that have reported substantial deviations for higher-order statistics, see for example Frisch (1995) and Sreenivasan & Antonia (1997) and references therein. These deviations, known as anomalous scaling, occur even when the condition of sufficiently high Reynolds number is met and have their origin primarily in a phenomenon referred to as internal intermittency (Nelkin 1994). Internal intermittency describes a stochastic process, which exhibits very strong fluctuations that occur more frequently than predicted by a Gaussian distribution. These strong fluctuations are non-universal, which invalidates Kolmogorov's self-similarity hypotheses (Landau & Lifshitz 1963). Internal intermittency is created by the nonlinear dynamics of the vortex stretching mechanism and occurs predominantly at the small scales of any turbulent flow.

The concept of self-similarity has been established since the seminal work of Townsend (1951) as an important tool that is less restrictive than universality. Townsend (1951) postulated that turbulent flows approach a self-similarity solution when the large-scale structures in the near field break down and eventually develop an equilibrium state. It is now widely accepted that most turbulent shear flows reach a state in the far field in which certain low-order statistics become self-similar and are determined by a single set of characteristic length and velocity scales (Thiesset, Antonia & Djenidi 2014*a*; Djenidi *et al.* 2017). Self-similarity solutions are in general not universal, but depend on the initial or boundary conditions of the specific flow (George 2009). Moreover, many flows do not satisfy complete self-similarity for the entire range of scales (Meldi & Sagaut 2013). The term partial self-similarity refers to flows in which self-similarity is valid only for a restricted range of scales (Saffman 1967).

There are numerous studies that have approached turbulent flows from a self-similarity perspective. The first self-similarity study by von Kármán & Howarth (1938) presented solutions of correlation functions in decaying grid turbulence. The analysis of von Kármán & Howarth (1938) was extended by George (1992) and Speziale & Bernard (1992), where it was shown that self-similarity implies a power-law decay of the mean turbulent energy $\langle k\rangle$. Later, Gonzalez & Fall (1998) noted that complete self-similarity requires that $\langle k\rangle \propto t^{-1}$, which in turn implies that the turbulent Reynolds number stays constant during the evolution of the flow. Some flows exhibit complete self-similarity in the far field, such as the turbulent round jet (Thiesset *et al.* 2014*a*) or the wake behind a circular cylinder (Tang *et al.* 2016). Complete self-similarity was also observed at the centreplane of a temporally evolving planar jet (Sadeghi, Oberlack & Gauding 2018), which is the flow considered in this study. In the context of structure functions, most self-similarity studies have been devoted to the centre of the jet (Pearson & Antonia 2001; Sadeghi, Lavoie & Pollard 2015).

https://doi.org/10.1017/jfm.2021.399 Published online by Cambridge University Press

However, the situation is more precarious and it is of interest to investigate whether self-similarity is restricted to the centreplane or if it is valid across the entire flow, particularly when considering self-similarity of higher-order structure functions. Turbulent jet flows are exposed to a complex phenomenon that is commonly referred to as external intermittency (Townsend 1949). External intermittency is the result of the manifestation of two different parts of the flow: the first is the fully developed turbulent core, and the second is the non-turbulent outer field, which is associated with negligible vorticity fluctuations (da Silva *et al.* 2014). These two adjacent regions are divided by a sharp, highly contorted layer; the so-called turbulent/non-turbulent interface (TNTI). The TNTI leads to the appearance of alternating flow structures when the outer irrotational fluid is mixed with highly turbulent fluid (Westerweel *et al.* 2009). The TNTI has a finite thickness of typically 10 to 15 Kolmogorov lengths (Silva, Zecchetto & da Silva 2018). The outer-most layer of the TNTI is the so-called irrotational boundary (IB), which is easily detectable, and therefore used in this work to distinguish between turbulent and non-turbulent regions (da Silva & Pereira 2008; van Reeuwijk & Holzner 2014; Krug *et al.* 2017*a*,*b*). By analysing a variety of different free shear flows, Kuznetsov, Praskovsky & Sabelnikov (1992) showed that external intermittency can have an impact on the entire flow and, at least for flows at laboratory scale, can break small-scale universality. In particular, Mi & Antonia (2001) demonstrated that external intermittency can change the inertial subrange scaling exponents of structure functions and energy spectra in turbulent round jets. These observations give rise to the question of whether and how external and internal intermittency are coupled.

The objective of this paper is to study the combined impact of internal and external intermittency on small-scale turbulence in turbulent temporally evolving planar jet flows. The analysis is based on the self-similarity of low-order and higher-order velocity structure functions at different cross-wise positions in the jet flow. Specifically, the scaling of higher-order structure functions has unveiled intrinsic scale-sensitive features of intermittency (Kraichnan 1974; Anselmet *et al.* 1984). Recently, Yasuda & Vassilicos (2018) evaluated the impact of large-scale fluctuations on small-scale turbulence by the scale-by-scale energy budget equation, and Chien, Blum & Voth (2013) observed that the signature of large-scale fluctuations can be recovered in the scaling laws of structure functions.

The remainder of the paper is structured as follows. First, we introduce in § 2 the direct numerical simulation (DNS) of the turbulent jet flows on which the analysis is based. In § 3, we systematically study structure functions of different orders from the self-similarity and self-preservation perspective. The analysis is carried out at different locations in the jet (such as the centreplane and the shear layer) and for different Reynolds numbers. Constraints that structure functions must satisfy under the condition of complete self-preservation are derived. Afterwards, we investigate in § 4 the impact of external intermittency on the self-similarity of structure functions at different scales. Of particular interest is the question of whether and how internal and external intermittency are coupled. A conclusion is given in § 5.

2. Data-set description

2.1. *Problem formulation*

The subsequent analysis is based on data of highly resolved DNSs of temporally evolving planar jet flows at different Reynolds numbers. The DNS solves the incompressible

https://doi.org/10.1017/jfm.2021.399 Published online by Cambridge University Press

Navier–Stokes equations in non-dimensional form, given by

$$\left.\begin{aligned} \frac{\partial U_k}{\partial x_k} &= 0, \\ \frac{\partial U_j}{\partial t} + U_k \frac{\partial U_j}{\partial x_k} &= -\frac{\partial P}{\partial x_j} + \frac{1}{Re_0} \frac{\partial^2 U_j}{\partial x_k \partial x_k}, \quad j = 1, 2, 3, \end{aligned}\right\} \tag{2.1}$$

where $\boldsymbol{U}$ denotes the velocity vector with components $(U_1, U_2, U_3)^\intercal$ in the streamwise, spanwise and cross-wise directions, respectively, and P is the pressure. The corresponding fluctuating fields will be denoted by $\boldsymbol{u} = (u_1, u_2, u_3)^\intercal$ and p. The dependent variables are functions of space $\boldsymbol{x} = (x_1, x_2, x_3)^\intercal$ and time t. Further, Einstein's summation convention is used, which implies summation over indices appearing twice. All quantities are non-dimensionalized by the initial centreplane mean velocity U_0 and the initial jet thickness H_0. The jet thickness H_0 is defined as the distance over which the mean velocity profile decreases to half of its centreplane value. Without loss of generality, H_0 and U_0 are set to unity. The initial Reynolds number is defined as

$$Re_0 = \frac{U_0 H_0}{\nu}, \tag{2.2}$$

with ν being the kinematic viscosity. Four different jet flows with Re_0 chosen as 1000, 2000, 5000 and 10 000 are studied in this paper.

The DNS was carried out on the supercomputer JUQUEEN (Stephan & Docter 2015) with the in-house solver psOpen (Gauding *et al.* 2014, 2019; Hunger, Gauding & Hasse 2016; Sadeghi *et al.* 2018). In order to obtain a high accuracy, spatial derivatives are computed by a sixth-order Padé scheme with spectral-like accuracy (Lele 1992). Temporal integration is performed by a low storage, stability-preserving fourth-order Runge–Kutta scheme. The Poisson equation is efficiently solved in spectral space by employing a Helmholtz equation (Mellado *et al.* 2010; Mellado & Ansorge 2012). To reduce aliasing errors, the nonlinear terms are formulated in skew-symmetric form (Erlebacher *et al.* 1990), and additionally, a sixth-order compact filter is applied.

The rectangular computational domain has periodic boundary conditions in the streamwise and spanwise directions (denoted by x_1 and x_2), and free-slip boundary conditions in cross-wise direction (denoted by x_3). The jet flow is statistically homogeneous in the (x_1, x_2)-planes, and the jet grows with time t in the cross-wise direction x_3. Statistics are computed over (x_1, x_2)-planes and depend only on time and the cross-wise coordinate x_3. Furthermore, statistical symmetry with respect to the midplane is exploited to improve the quality of statistical quantities. Ensemble averages computed over these planes are denoted by angular brackets. The statistical quality of ensemble averages is discussed in Appendix A.

The governing equations are solved in a computational domain of size $L_1/H_0 = 20$, $L_2/H_0 = 20$ and $L_3/H_0 = 12$, discretized on a mesh with up to $5376 \times 5376 \times 2688$ grid points. The size of the computational domain is sufficiently large compared with the integral scales, firstly, to avoid confinement effects when the thickness of the jet increases with time, and secondly, to improve the quality of statistical quantities. A uniform equidistant mesh is used for the inner part of the domain, while the outer part is increasingly coarsened toward the boundaries. The grid width is chosen such that it is everywhere smaller than the Kolmogorov length scale. This feature of the DNS is especially important for the accurate evaluation of higher-order statistics in the dissipative range (Watanabe & Gotoh 2007).

https://doi.org/10.1017/jfm.2021.399 Published online by Cambridge University Press

Case	Grid	Re_0	Re_λ	$h_{1/2}$
A	$1536 \times 1536 \times 768$	1000	35	1.17
B	$2048 \times 2048 \times 1024$	2000	51	1.16
C	$3072 \times 3072 \times 1536$	5000	74	1.15
D	$5376 \times 5376 \times 2688$	10 000	107	1.16

Table 1. Characteristic properties of four different jet flows (denoted by cases A–D) at time $t = 23.3$ with Reynolds numbers Re_0 between 1000 and 10 000. Here, Re_λ refers to the Taylor-based Reynolds number at the centreplane.

	t	$h_{1/2}$	U_c	Re_λ	$\langle k \rangle \times 10^2$	$\langle \varepsilon \rangle \times 10^3$
D1	13.2	0.86	0.57	105.2	2.87	4.98
D2	15.5	0.93	0.52	105.8	2.39	3.40
D3	18.0	1.00	0.48	105.6	2.02	2.43
D4	20.6	1.06	0.45	107.1	1.76	1.80
D5	23.3	1.16	0.42	107.4	1.57	1.39

Table 2. Characteristic properties of case D ($Re_0 = 10\,000$) at the centreplane at five different times (denoted by D1–D5) displayed in figure 1.

An appropriate initialization of the DNS is necessary. Following da Silva & Pereira (2008), the initial velocity profile is composed of two mirrored hyperbolic-tangent mean profiles and perturbed by broadband random Gaussian fluctuations that follow a prescribed energy spectrum. The turbulent intensity u'/U_0, with u' being the root mean square of the velocity, equals approximately 2 % to facilitate a rapid transition to fully developed turbulence.

2.2. *Characteristic properties of the DNS*

The turbulent jet flows used in this study are now briefly characterized. The analysis is carried out for four different jet Reynolds numbers between 1000 and 10 000 (denoted by cases A to D). The case D with the highest Reynolds number is taken as reference case, which is additionally studied at five different times (denoted by D1 to D5). The analysis is conducted in the far field of the jet for t between $t = 13.2$ and $t = 23.3$. Characteristic parameters of the DNS are summarized in tables 1 and 2.

In the remainder of this section, we present the temporal evolution of different statistics at the centreplane. Figure 1 displays for case D the evolution of the mean kinetic energy $\langle k \rangle = \langle u_i^2 \rangle / 2$ and the mean dissipation rate $\langle \varepsilon \rangle = 2\nu \langle S_{ij}^2 \rangle$, with

$$S_{ij} = \frac{1}{2}\left(\frac{\partial u_i}{\partial x_j} + \frac{\partial u_j}{\partial x_i}\right) \tag{2.3}$$

being the strain-rate tensor. It can be observed that $\langle k \rangle$ and $\langle \varepsilon \rangle$ reveal a power-law decay with scaling exponents close to -1 and -2, respectively, which is consistent with analytical solutions for complete self-similarity (Gonzalez & Fall 1998; Sadeghi *et al.* 2018). To proceed further, let $u_k = (\nu \langle \varepsilon \rangle)^{1/4}$ denote the Kolmogorov velocity and $u' = (2\langle k \rangle / 3)^{1/2}$ the root mean square of the velocity. From these velocity scales,

https://doi.org/10.1017/jfm.2021.399 Published online by Cambridge University Press

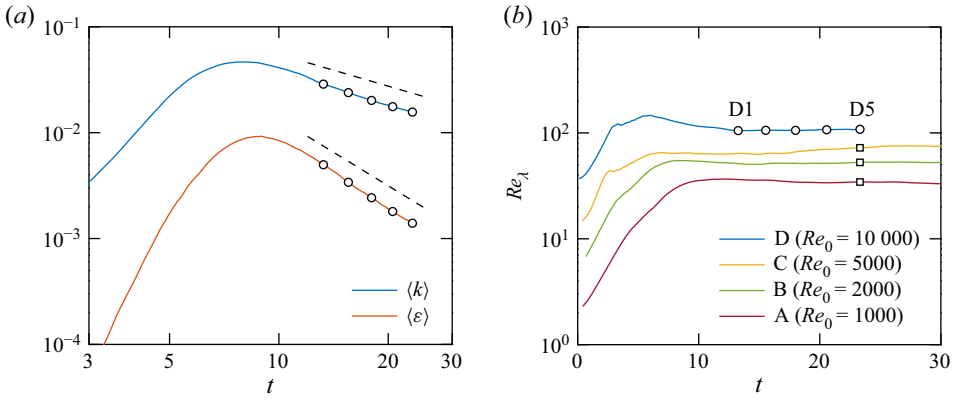

Figure 1. (*a*) Temporal evolution of the mean turbulent kinetic energy $\langle k \rangle$ as well as the mean energy dissipation rate $\langle \varepsilon \rangle$ at the centreplane for case D. The black dashed lines indicate a power-law decay with t^{-1} and t^{-2}, respectively. (*b*) Temporal evolution of the Taylor micro-scale-based Reynolds number Re_λ for cases A–D. The circles specify different times (D1–D5) that are used for the self-preservation analysis. The squares represented additional data used to study the variation of the jet Reynolds number Re_0.

the Taylor-scale Reynolds number

$$Re_\lambda = \sqrt{15}\frac{u'^2}{u_k^2} \tag{2.4}$$

can be built. The Taylor-scale Reynolds number approaches approximately a constant value, which is between 35 and 107 for the four different simulations considered. In Appendix B, we demonstrate that a constant Reynolds number is a necessary condition for the self-similarity of jet flows.

With a constant Reynolds number, all length and velocity scales follow exactly the same scaling during the decay. Figure 2 shows the temporal evolution of the jet half-width $h_{1/2}$ (defined as the distance from the centreplane over which the mean streamwise velocity decreases to the half of the centreplane value U_c), the Taylor micro-scale $\lambda = (15\nu u'^2/\langle\varepsilon\rangle)^{1/2}$, the Kolmogorov length scale $\eta = (\nu^3/\langle\varepsilon\rangle)^{1/4}$ as well as the velocity scales U_c, u' and u_k. It can be observed that the length scales increase as $t^{1/2}$, and at the same time, the velocity scales decrease as $t^{-1/2}$. Also, the outer scales $h_{1/2}$ and U_c follow the same scaling laws, see Appendix B for the derivation.

3. Self-similarity and self-preservation of planar jet flows

We start the analysis by introducing the nth-order velocity structure function as

$$S_n = \langle \Delta u_1^n \rangle, \tag{3.1}$$

where $\Delta u_1 = u_1(\boldsymbol{x} + r\boldsymbol{e}_1, t) - u_1(\boldsymbol{x}, t)$ is the longitudinal velocity increment in streamwise direction, r is the separation distance between the two points considered and $\boldsymbol{e}_1$ is a unit vector in the streamwise direction. In order to explore conditions under which S_n admits self-similarity, we introduce the functional form

$$S_n(r; t, \hat{x}_3, Re_0) = u_{ref}^n(t, \hat{x}_3, Re_0) f_n(\hat{r}), \tag{3.2}$$

which is built with a characteristic velocity scale u_{ref} and a non-dimensional, order-dependent shape function f_n. Essentially, (3.2) introduces a separation of variables,

https://doi.org/10.1017/jfm.2021.399 Published online by Cambridge University Press

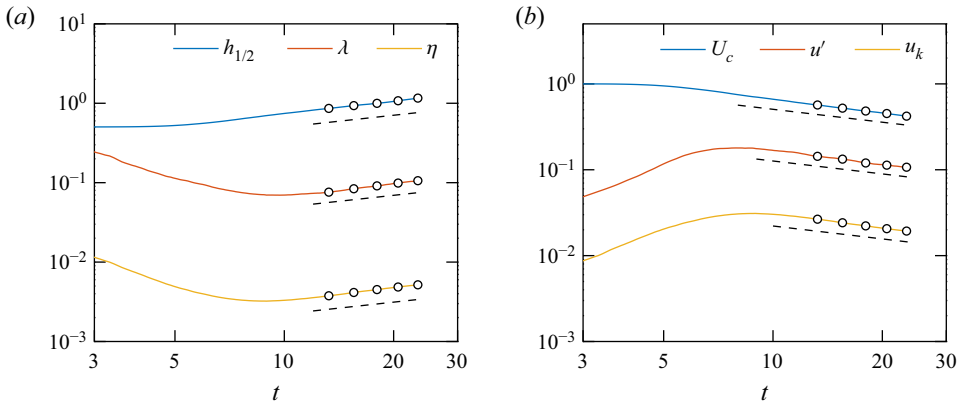

Figure 2. (*a*) Temporal evolution of the length scales $h_{1/2}$, λ and η (*a*), where the dashed lines indicate the self-similarity solution with $t^{1/2}$, and (*b*) temporal evolution of the velocity scales U_c, u' and u_k, where the dashed lines represent the self-similarity solution with $t^{-1/2}$. The circles indicate different times that are used for the further analysis. Data presented for case D.

where only the shape function f_n, and not the prefactor u_{ref}, depends on the normalized separation distance $\hat{r}$, defined as $\hat{r} = r/L_{ref}(t)$ with $L_{ref}(t)$ being a characteristic length scale. Equation (3.2) is a function of additional external parameters, namely the time t, the jet Reynolds number Re_0 and the cross-wise position $\hat{x}_3 = x_3/h_{1/2}(t)$. It should be noted that (3.2) postulates the existence of a single set of characteristic length and velocity scales. The validity of this assumption is discussed in the next section.

Different special cases can be deduced from (3.2). The case of self-similarity with respect to time will be referred to as self-preservation. Complete self-preservation occurs when the normalized structure functions $S_n(r; t, \hat{x}_3, Re_0)/u^n_{ref}(t, \hat{x}_3, Re_0)$ collapse at fixed $\hat{x}_3$ and Re_0 over the entire r space for any time t. In a similar fashion, self-similarity with respect to the cross-wise position $\hat{x}_3$ and the Reynolds number Re_0 can be defined.

In what follows, we derive analytical constraints for the self-preservation of structure functions of any even order without using any *ad hoc* assumptions. After that, the self-similarity and self-preservation of structure functions is systematically tested by varying the arguments of (3.2). Also, we would like to mention that, unlike Kolmogorov's K41 theory, the self-similarity and self-preservation analysis does not require a high Reynolds number (Antonia *et al.* 2003).

3.1. *Analytical similarity solutions of structure functions*

Analytical solutions of structure functions exist in the asymptotic small-scale and large-scale limits and can be used to derive conditions for self-similarity and self-preservation. In the small-scale limit, a Taylor series expansion of $\langle \Delta u_1^{2n} \rangle$ gives

$$\langle \Delta u_1^{2n} \rangle = \left\langle \left(\frac{\partial u_1}{\partial x_1} \right)^{2n} \right\rangle r^{2n} + O(r^{2n+2}), \tag{3.3}$$

where the series is truncated after the first non-negative term. Normalizing (3.3) with the Kolmogorov scales gives the expression

$$\frac{\langle \Delta u_1^{2n} \rangle}{u_k^{2n}} = \frac{F^<_{2n} R_\varepsilon}{15^n} \left(\frac{r}{\eta} \right)^{2n}. \tag{3.4}$$

https://doi.org/10.1017/jfm.2021.399 Published online by Cambridge University Press

The right-hand side of (3.4) depends on two external parameters, $F_{2n}^{<}$ and R_ε, as well as the universal shape function $(r/\eta)^{2n}$. The first external parameter in (3.4) is the non-dimensional moment of the streamwise velocity gradient

$$F_{2n}^{<} = \frac{\left\langle \left(\dfrac{\partial u_1}{\partial x_1} \right)^{2n} \right\rangle}{\left\langle \left(\dfrac{\partial u_1}{\partial x_1} \right)^{2} \right\rangle^{n}}, \tag{3.5}$$

which quantifies intermittent fluctuations of the velocity gradient field (Frisch 1995; Sreenivasan & Antonia 1997). The second parameter

$$R_\varepsilon = \frac{15\nu}{\langle \varepsilon \rangle} \left\langle \left(\frac{\partial u_1}{\partial x_1} \right)^{2} \right\rangle \tag{3.6}$$

quantifies the departure from small-scale isotropy and equals unity under local isotropy. Equation (3.4) is an exact generalization of Kolmogorov's first scaling hypothesis (Kolmogorov 1941*b*) to anisotropic turbulence with internal intermittency (Boschung *et al.* 2016). Alternatively, structure functions can be normalized with the Taylor scales u' and λ, which gives with (3.3) the expression

$$\frac{\langle \Delta u_1^{2n} \rangle}{u'^{2n}} = F_{2n}^{<} R_\varepsilon \left(\frac{r}{\lambda} \right)^{2n}. \tag{3.7}$$

Essentially, (3.4) and (3.7) are analytical solutions for $\langle \Delta u_1^{2n} \rangle$ in the dissipative range that account for both anisotropy and intermittency. Independent of the chosen set of length and velocity scales, self-preservation of structure functions at the small scales requires that the product of $F_{2n}^{<}$ and R_ε is invariant with time (note that $F_2^{<}$ equals unity, and hence the constancy of R_ε is sufficient for the second order).

Analytical solutions for structure functions also exist in the large-scale limit. In statistically homogeneous turbulence, structure functions become independent of the separation distance when r is larger than the integral length scale. The limiting value can be obtained from the binomial theorem and equals

$$\langle \Delta u_1^{2n} \rangle = \sum_{k=0}^{2n} \binom{2n}{k} (-1)^k \langle u_1^{2n-k} \rangle \langle u_1^{k} \rangle. \tag{3.8}$$

To proceed, we exploit the fact that all odd moments of u_1 vanish at the centreplane due to symmetry. In that case, (3.8) simplifies to

$$\langle \Delta u_1^{2n} \rangle = \sum_{k=0}^{n} \frac{(2n)!}{(2k)!(2n-2k)!} \langle u_1^{2n-2k} \rangle \langle u_1^{2k} \rangle. \tag{3.9}$$

By introducing the non-dimensional moments of the velocity fluctuations

$$F_{2n}^{>} = \frac{\langle u_1^{2n} \rangle}{\langle u_1^{2} \rangle^{n}}. \tag{3.10}$$

https://doi.org/10.1017/jfm.2021.399 Published online by Cambridge University Press

Equation (3.9) can be rewritten as

$$\langle \Delta u_1^{2n} \rangle = \langle u_1^2 \rangle^n \sum_{k=0}^{n} \frac{(2n)!}{(2k)!(2n-2k)!} F_{2n-2k}^{>} F_{2k}^{>} = \langle u_1^2 \rangle^n C_{2n}, \tag{3.11}$$

where the prefactor C_{2n} relates the large-scale limit of any order structure function to the variance $\langle u_1^2 \rangle$. For instance, from (3.11) we find that $\langle \Delta u_1^2 \rangle$ approaches $2\langle u_1^2 \rangle$, and $\langle \Delta u_1^4 \rangle$ approaches $2(F_4^{>} + 3)\langle u_1^2 \rangle^2$. Further, we introduce a large-scale anisotropy parameter R_u as

$$\langle u_1^2 \rangle = R_u u'^2, \tag{3.12}$$

which equals unity for isotropic turbulence. With these definitions, the large-scale limit of $\langle \Delta u_1^{2n} \rangle$ becomes, after normalization with the Kolmogorov scales,

$$\frac{\langle \Delta u_1^{2n} \rangle}{u_k^{2n}} = 15^{-n/2} C_{2n} R_u^n Re_\lambda^n, \tag{3.13}$$

and after normalization with the Taylor scales

$$\frac{\langle \Delta u_1^{2n} \rangle}{u'^{2n}} = C_{2n} R_u^n. \tag{3.14}$$

Self-preservation of the structure functions at the large scales requires hence the constancy of the right-hand sides of (3.13) and (3.14).

The analysis presented provides certain constraints for self-preservation that structure functions of different order must satisfy. For second-order structure functions, the only requirement for self-preservation is the constancy of the anisotropy factors R_u and R_ε during the evolution of the jet as $F_2^{<}$ and $F_2^{>}$ equal unity by definition, see (3.4), (3.7), (3.13) and (3.14). An important consequence is that isotropy is not required for the validity of self-preservation and any anisotropy that is present in the flow must persist indefinitely. In other words, a return to isotropy is not consistent with self-preservation. The persistence of anisotropy has been also postulated in the context of self-similarity of turbulent wakes by Thiesset, Danaila & Antonia (2013*b*).

Knowing that the anisotropy factors R_u and R_ε must stay constant for self-preservation, the analysis provides additional constraints for higher-order structure functions. More specifically, (3.4), (3.7), (3.13) and (3.14) require that the non-dimensional moments $F_{2n}^{<}$ and $F_{2n}^{>}$ remain constant for self-preservation. This condition is valid for any even order. It should be noted that the constancy of the flatness factors can be also inferred from the constancy of the Reynolds number (Schumacher *et al.* 2014) in completely self-preserving flows.

Table 3 lists for case D the aforementioned parameters at the centreplane during the evolution of the jet. The flatness factor $F_4^{>}$ is close to 2.9, which indicates that velocity fluctuations in the core of the jet follow approximately a Gaussian distribution. The flatness of the velocity gradients $F_4^{<}$ is close to 6, which reflects departures from Gaussianity due to intermittency. Table 3 shows that the anisotropy factors R_u and R_ε also stay nearly constant during the decay of the jet. Small-scale isotropy is fulfilled within less than two per cent deviation, while the departure from large-scale isotropy reaches approximately ten per cent. Furthermore, table 3 shows that the skewness of the velocity fluctuations, defined as $S_u = \langle u_1^3 \rangle / \langle u_1^2 \rangle^{3/2}$, remains close to zero at the centreplane, as required by symmetry.

https://doi.org/10.1017/jfm.2021.399 Published online by Cambridge University Press

	D1	D2	D3	D4	D5
$F_4^<$	6.068	5.910	6.057	5.919	5.883
$F_4^>$	2.872	2.837	2.918	2.875	2.889
S_u	0.040	0.031	0.024	−0.020	−0.024
R_ε	0.997	0.989	0.991	0.984	0.987
R_u	1.074	1.110	1.071	1.090	1.099

Table 3. Temporal evolution of different quantities at the centreplane of case D, i.e. the velocity gradient flatness $F_4^<$, the flatness of the velocity fluctuations $F_4^>$, the skewness of the velocity fluctuations $S_u = \langle u_1^3\rangle/\langle u_1^2\rangle^{3/2}$ as well as the anisotropy coefficients R_ε and R_u, characterizing the small- and large-scale anisotropy, respectively.

3.2. *Self-preservation of structure functions at the centreplane*

Let us now examine whether structure functions are self-preserving at the centreplane. The analysis is conducted for the even-order longitudinal structure functions up to the sixth order. Higher-order structure functions are of interest because they provide information about intermittency (Pearson & Antonia 2001). The characteristic scales u_{ref} and L_{ref} are chosen as (1) the Kolmogorov scales u_k and η, (2) the Taylor scales u' and λ and (3) the outer scales U_c and $h_{1/2}$. Once the jet flow has reached a constant Reynolds number, the inner scales (Kolmogorov or Taylor scales) should be exchangeable with the outer scales (U_c and $h_{1/2}$). This assertion is tested now using the DNS data.

Figure 3 shows $f_2(\hat{r})$, $f_4(\hat{r})$ and $f_6(\hat{r})$ at the centreplane ($\hat{x}_3 = 0$) for $Re_0 = 10\,000$ at five different times (D1–D5). It can be seen that the normalized structure functions admit complete self-preservation, which means that the normalized structure functions collapse for any time t over the entire r space. Hence, complete self-preservation is valid regardless of the order and the chosen set of reference scales. It should be mentioned that complete self-preservation of second-order structure functions has also been reported by Tang *et al.* (2016) and Thiesset *et al.* (2014*a*) at the centre of round jets.

Complete self-preservation is a direct consequence of the constant centreplane Reynolds number. At a constant Reynolds number, the ratio between large-scale and small-scale quantities remains unchanged with time and any set of length and velocity scales can be chosen as reference scales. In that case, self-preservation of structure functions is not only valid for the second order but valid for any higher order.

3.3. *Self-preservation of structure functions in the shear region*

At the centre of the jet, turbulence statistics are close to those observed in homogeneous isotropic decaying turbulence (Antonia *et al.* 2003; Sinhuber, Bodenschatz & Bewley 2015). In this section, we examine whether structure functions still admit complete self-preservation away from the centre of the jet, where turbulence is affected by a mean shear or inhomogeneity and anisotropy effects (Casciola *et al.* 2003; Thiesset *et al.* 2014*b*).

To this end, we examine the self-preservation of the normalized structure functions in the shear layer of the jet at the position $x_3 = h_{1/2}$. At this position, the mean shear $\partial\langle U_1\rangle/\partial x_3$ is close to its maximum. Figure 4 presents for case D the corresponding structure functions up to the sixth order after normalization with the Kolmogorov scales (1), the Taylor scales (2) and the outer scales (3). Again, a perfect collapse can be observed over the entire range of scales for each order, regardless of the chosen set of scales for normalization. Hence, by comparison with figure 3, we can conclude that complete

https://doi.org/10.1017/jfm.2021.399 Published online by Cambridge University Press

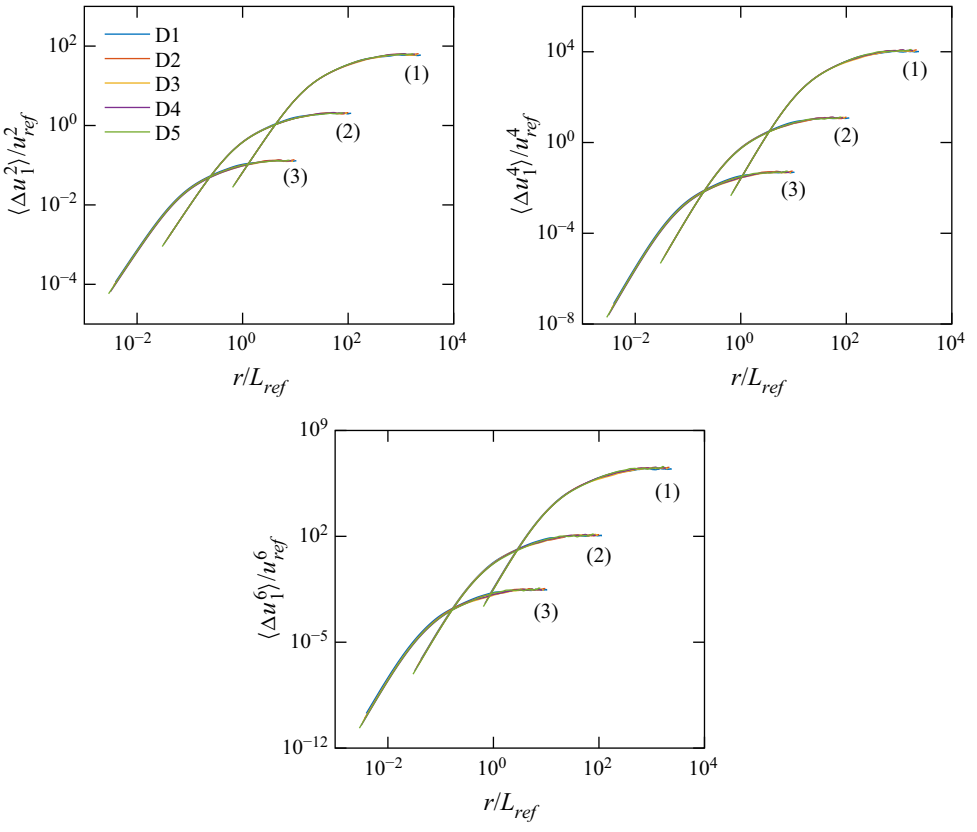

Figure 3. Self-preservation of even-order structure functions up to the sixth order at the centre of the jet ($\hat{x}_3 = 0$). The structure functions are normalized by the Kolmogorov scales (1), the Taylor scales (2) and the outer scales (3) and presented at different times (D1–D5).

self-preservation of structure functions is not limited to the core of the jet, but also valid in the shear layer.

3.4. *Impact of the initial conditions on the self-similarity of structure functions*

In the spirit of Kolmogorov's similarity theory, it is of interest to study the influence of a variation of the jet Reynolds number Re_0 on the self-similarity of the structure functions. To this end, we examine whether the normalized structure functions $S_n(\hat{r}; t, \hat{x}_3, Re_0)/u_{ref}^n(t, \hat{x}_3, Re_0)$ collapse over the entire r space when the jet Reynolds number Re_0 is changed and the other parameters are kept constant. To answer this question, we examine different jet flows with variations of the Reynolds number Re_0 between 1000 and 10 000, cf. table 1.

Figure 5 presents the second-order structure functions for these different jet Reynolds numbers at the centreplane. As expected, the structure functions do not satisfy self-similarity over the entire range of scales, neither after normalization with the Kolmogorov scales nor with the Taylor scales. Instead, the collapse with the Kolmogorov scales is restricted to the dissipative range, while the Taylor scales lead to a collapse only in the dissipative range and at the large scales, but not at intermediate scales. This finding confirms the standard understanding of turbulence that, in general, and specifically at low

https://doi.org/10.1017/jfm.2021.399 Published online by Cambridge University Press

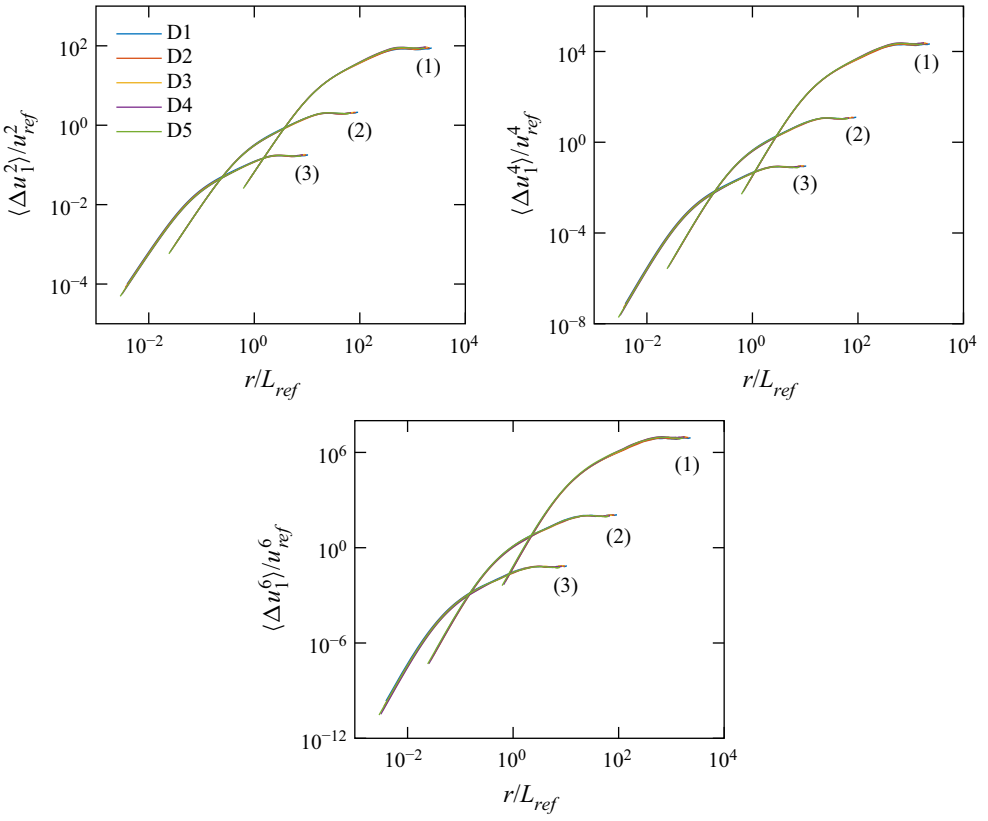

Figure 4. Self-preservation of even-order structure functions up to the sixth order at the edge of the jet at $x_3 = h_{1/2}$. At this position, the mean shear $\partial\langle U_1\rangle/\partial x_3$ is close to its maximum. The structure functions are normalized by the Kolmogorov scales (1), the Taylor scales (2) and the outer scales (3) and presented at different times (D1–D5).

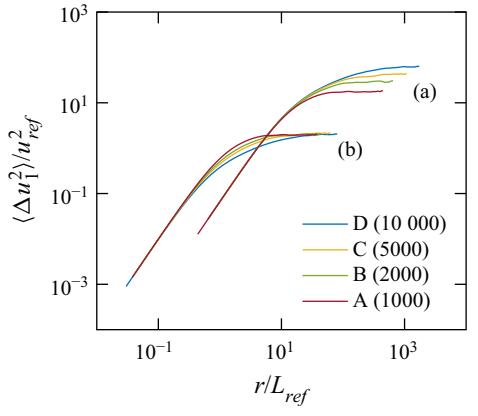

Figure 5. Normalized second-order structure functions at the centreplane for different Reynolds numbers between 1000 and 10 000. The structure functions are normalized by Kolmogorov scales (a) and Taylor scales (b).

https://doi.org/10.1017/jfm.2021.399 Published online by Cambridge University Press

to moderate Reynolds numbers, structure functions do not feature universality over the entire range of scales (Pearson & Antonia 2001). Moreover, figure 5 supports the claim that a constant turbulent Reynolds number is a necessary condition for complete self-similarity or self-preservation of structure functions.

It is important to note that by virtue of self-preservation, the results presented are invariant with time once the far field of the jet is reached.

4. The effect of external intermittency

In this section, we examine whether structure functions $S_n(r; \hat{x}_3, t, Re_0)$ admit self-similarity when the cross-wise position $\hat{x}_3 = x_3/h_{1/2}$ is varied and discuss which role external intermittency plays.

4.1. *The TNTI*

External intermittency can be evaluated by the intermittency – or indicator – function Γ, defined as

$$\Gamma(\boldsymbol{x}, t) = H(\omega^2(\boldsymbol{x}, t) - \omega_0^2), \tag{4.1}$$

where H is the Heaviside function, ω^2 is the enstrophy and ω_0^2 is a threshold value of the enstrophy that defines the position of the IB. The intermittency factor

$$\gamma(x_3, t) = \langle \Gamma(\boldsymbol{x}, t) \rangle, \tag{4.2}$$

quantifies the probability that the flow at a certain cross-wise position x_3 is turbulent (Townsend 1949). Since the IB is a singular surface, the flow field can be partitioned into two states, either turbulent if $\omega^2 > \omega_0^2$, or non-turbulent in any other case. With this definition, any conventionally averaged quantity $\langle \Psi \rangle$ can be decomposed as

$$\langle \Psi \rangle = \gamma \langle \Psi \rangle_t + (1 - \gamma) \langle \Psi \rangle_n, \tag{4.3}$$

where $\langle \Psi \rangle_t$ and $\langle \Psi \rangle_n$ indicate conditional averages that consider either turbulent and non-turbulent events, respectively (Mellado, Wang & Peters 2009). With the binary indicator function Γ, the conditional averages are defined as

$$\langle \Psi \rangle_t = \langle \Gamma \Psi \rangle \quad \text{and} \quad \langle \Psi \rangle_n = \langle (1 - \Gamma) \Psi \rangle. \tag{4.4a,b}$$

It is now widely accepted that the IB can be defined by an appropriate threshold of the enstrophy (Bisset, Hunt & Rogers 2002; Holzner *et al.* 2008; da Silva & Pereira 2008; da Silva *et al.* 2014; Silva *et al.* 2018; Watanabe, da Silva & Nagata 2019). The threshold value ω_0^2 is systematically obtained from the probability density function (p.d.f.) of $\log_{10}(\omega^2/\hat{\omega}^2)$. Following Krug *et al.* (2017*a*), the local enstrophy field is normalized by $\hat{\omega}^2$, defined as

$$\hat{\omega}^2 = \frac{\displaystyle\int_{-\infty}^{\infty} \langle \omega^2 \rangle^2 \, \mathrm{d}x_3}{\displaystyle\int_{-\infty}^{\infty} \langle \omega^2 \rangle \, \mathrm{d}x_3}, \tag{4.5}$$

to remove the time dependence from the threshold criterion. Figure 6(*a*) displays the p.d.f. of $\log_{10}(\omega^2/\hat{\omega}^2)$ at different times. In flows exposed to external intermittency, the p.d.f. exhibits a bimodal shape, where the two peaks that represent turbulent and non-turbulent regions are clearly separated by several orders of magnitude. In this work, we chose a

https://doi.org/10.1017/jfm.2021.399 Published online by Cambridge University Press

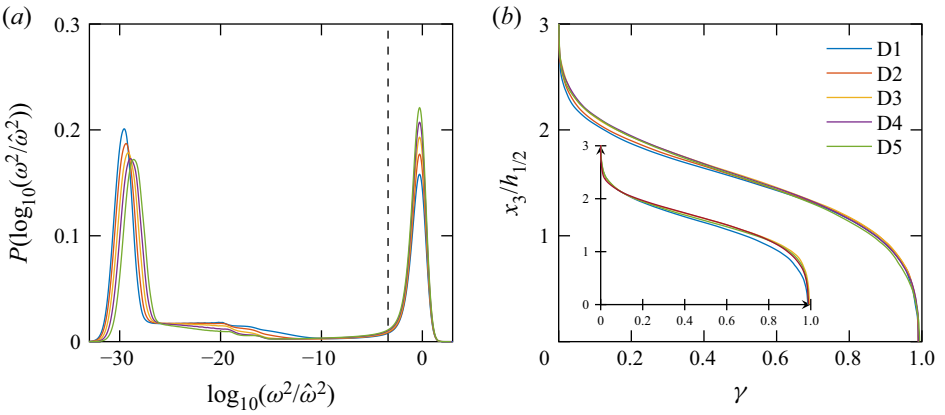

Figure 6. (*a*) The p.d.f. of $\log_{10}(\omega^2/\hat{\omega}^2)$ at different times for case D. The dashed vertical line indicates the threshold $\log_{10}(\omega_0^2/\hat{\omega}^2) = -3.4$. (*b*) Variation of the intermittency factor γ with the cross-wise coordinate $\hat{x}_3$ at different times (D1–D5) and jet Reynolds numbers Re_0 between 1000 and 10 000 (inset).

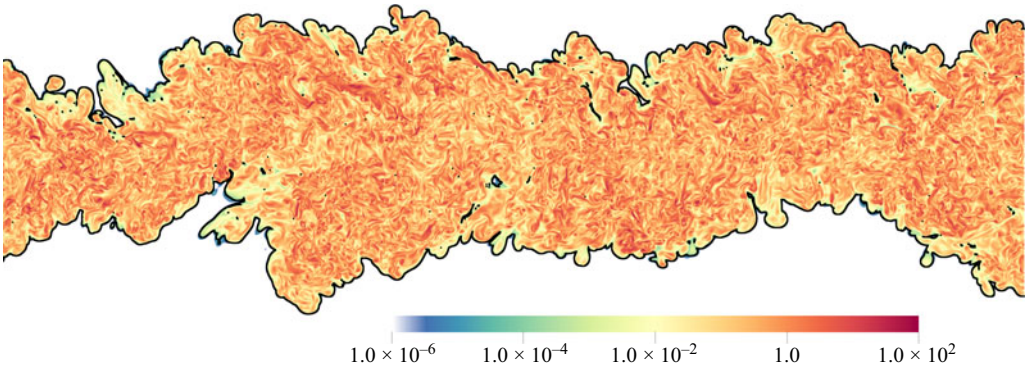

Figure 7. Visualization of the enstrophy field $\omega^2/\hat{\omega}^2$ for case D5 in a (x_1, x_3)-plane. The black contour line represents the IB defined by the enstrophy criterion $\log_{10}(\omega_0^2/\hat{\omega}^2) = -3.4$.

threshold $\log_{10}(\omega_0^2/\hat{\omega}^2) = -3.4$ for all cases. The enstrophy sharply increases across the TNTI, which makes the position of the IB reasonably insensitive regarding the exact threshold value (Krug *et al.* 2017*b*; Elsinga & da Silva 2019). The visualization of the enstrophy field and the IB in figure 7 indicates that the threshold is suitably chosen to distinguish between turbulent and non-turbulent regions. Furthermore, the sensitivity of the reported results with respect to the value of the threshold is examined in Appendix A.

Figure 6(*b*) shows the variation of the intermittency factor γ with the cross-wise coordinate $\hat{x}_3$ for different time steps and Reynolds numbers. At the centre, there is an almost fully turbulent region with γ close to unity that extends up to $\hat{x}_3 \approx 0.5$. At the edge of the flow, a steep decrease of γ is visible. It originates from an alternating flow structure, when the outer fluid with low vorticity is mixed with highly turbulent fluid from the core region of the jet. A visualization of this flow structure is shown in Appendix C. It is also worth mentioning that γ is approximately self-preserving and independent of the Reynolds number when plotted as a function of $\hat{x}_3$.

In the next section, the intermittency structure function is introduced to evaluate the morphology of the IB at different scales.

https://doi.org/10.1017/jfm.2021.399 Published online by Cambridge University Press

4.2. *Intermittency structure function*

In turbulent flows exposed to external intermittency, there are three different possibilities for the distribution of the ending points $\boldsymbol{x}$ and $\boldsymbol{x} + r\boldsymbol{e}_1$ of the velocity increments $\Delta u_1 = u_1(\boldsymbol{x} + r\boldsymbol{e}_1, t) - u_1(\boldsymbol{x}, t)$ along a straight line. More precisely, both points can be either located within the turbulent or within the non-turbulent regime or one point may be in the turbulent and the other point in the non-turbulent regime. Kuznetsov *et al.* (1992) predicted the corresponding probabilities as $\gamma_{tt} = \gamma - \frac{1}{2}D_{\Gamma,IB}$, $\gamma_{nn} = 1 - \gamma - \frac{1}{2}D_{\Gamma,IB}$ and $\gamma_{nt} = D_{\Gamma,IB}$, where

$$D_{\Gamma,IB}(r; x_3, t) = \langle (\Gamma(\boldsymbol{x} + r\boldsymbol{e}_1, t) - \Gamma(\boldsymbol{x}, t))^2 \rangle \tag{4.6}$$

is the intermittency structure function. The probabilities satisfy the identity

$$\gamma_{tt} + \gamma_{nn} + \gamma_{nt} = 1. \tag{4.7}$$

The ratio

$$\frac{\gamma_{tt}}{\gamma} = 1 - \frac{D_{\Gamma,IB}}{2\gamma} \tag{4.8}$$

measures the conditional probability that one point of the increment

$$\Delta\Gamma = \Gamma(\boldsymbol{x} + r\boldsymbol{e}_1, t) - \Gamma(\boldsymbol{x}, t) \tag{4.9}$$

is in the turbulent regime given that the other point is also in a turbulent regime. In other words, $D_{\Gamma,IB}$ provides scale-sensitive information regarding the structure of the IB. Figure 8(*a*) shows γ_{tt}/γ at different cross-wise positions $\hat{x}_3$ varying between the centreplane and $\hat{x}_3 = 1.59$ for case D5 as a representative case. It can be observed that in the proximity of the centreplane (i.e. for $0 \leq \hat{x}_3 \leq 0.58$), γ_{tt}/γ is close to unity and nearly independent of the separation distance r, which reflects the fact that the core region of the jet is fully turbulent. Toward the edge of the jet, γ_{tt}/γ equals unity only for $r \to 0$, and decreases quickly at larger separation distances. This decrease comes from the alternation between turbulent and non-turbulent fluid and represents external intermittency.

To proceed further, we introduce the one-dimensional random telegraphic signal Γ_T as a model for the intermittency function Γ. The telegraphic signal Γ_T alternates randomly between 0 (non-turbulent) and 1 (turbulent) and the corresponding probabilities are defined as $p(\Gamma_T = 0) = 1 - \gamma$ and $p(\Gamma_T = 1) = \gamma$. Thiesset *et al.* (2020) showed that the random telegraphic signal has an analytical structure function, i.e.

$$D_{\Gamma,T}(r) = 2\gamma(1 - \gamma)[1 - \mathrm{e}^{-r/\mathcal{L}_T}], \tag{4.10}$$

where $\mathcal{L}_T$ is a characteristics length scale

$$\mathcal{L}_T = 2\gamma(1 - \gamma)\left[\lim_{r\to 0} \frac{D_{\Gamma,T}(r)}{r}\right]^{-1}, \tag{4.11}$$

which is related to the probability for a transition from 0 to 1 and *vice versa* (Fitzhugh 1983). The small-scale limit of the random telegraphic signal equals

$$\lim_{r\to 0} D_{\Gamma,T}(r) = 2\gamma(1 - \gamma)\frac{r}{\mathcal{L}_T} + O(r^2), \tag{4.12}$$

which signifies that $D_{\Gamma,T}$ is proportional to r when the separation distance is small compared with $\mathcal{L}_T$. It is important to note that (4.12) is fundamentally different from the

https://doi.org/10.1017/jfm.2021.399 Published online by Cambridge University Press

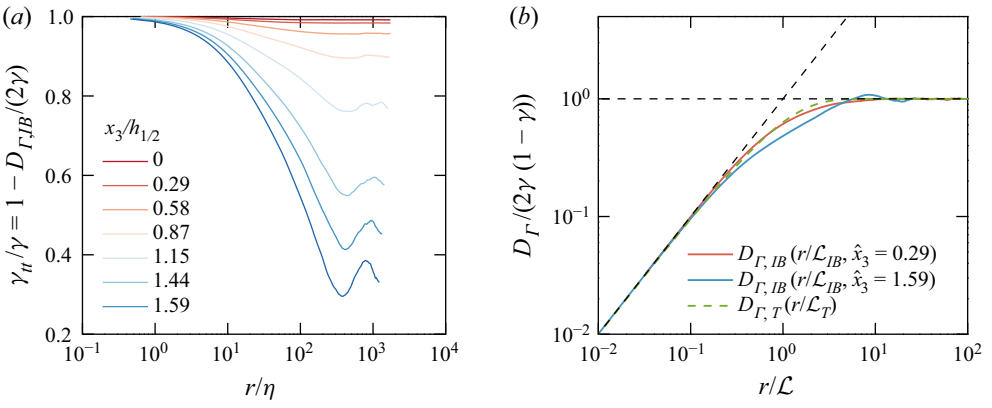

Figure 8. (*a*) Conditional probability γ_{tt}/γ at different cross-wise positions $\hat{x}_3$ (as indicated in the legend, $\hat{x}_3 = 0$ represents the centreplane). (*b*) Comparison of the structure function $D_{\Gamma,T}$ of a random telegraphic function (green dashed lines) with the intermittency structure function $D_{\Gamma,IB}$, shown for two different cross-wise positions $\hat{x}_3$ (solid red and blue lines). The black dashed lines indicate the analytical small-scale and large-scale limits. Data for case D5.

small-scale limit of velocity structure functions where $\langle \Delta u_1^2 \rangle \propto r^2$ applies. The different scaling is related to the fact that the velocity is a continuous field, while the intermittency function $\Gamma(\boldsymbol{x}, t)$ possesses discontinuities.

It is of interest to compare the analytical structure function of the random telegraphic signal $D_{\Gamma,T}$ with the intermittency structure function $D_{\Gamma,IB}$ of the turbulent jet. The intermittency structure function $D_{\Gamma,IB}$ is presented in figure 8(*b*) for two different cross-wise positions, normalized similar to (4.11) by the characteristic length scale

$$\mathcal{L}_{IB} = 2\gamma(1-\gamma)\left[\lim_{r\to 0}\frac{D_{\Gamma,IB}(r; x_3)}{r}\right]^{-1}, \tag{4.13}$$

and the large-scale limit $2\gamma(1-\gamma)$. Figure 8(*b*) reveals a perfect collapse between the DNS data and the random telegraphic function in the small-scale and large-scale limits. For intermediate scales, there is a growing discrepancy between $D_{\Gamma,T}$ and $D_{\Gamma,IB}$ with increasing distance from the centreplane. This difference is due to the fact that the morphology of the IB is not fully random, but instead determined by the dynamics of turbulence.

Let us now use the intermittency structure function to further examine the structure of the IB. Following Debye & Bueche (1949) and Debye, Anderson & Brumberger (1957), the small-scale limit of $D_{\Gamma,IB}$ can be expressed as

$$\lim_{r\to 0}\frac{D_{\Gamma,IB}}{r} = \left\langle \left| \frac{\partial \Gamma}{\partial x_1} \right| \right\rangle, \tag{4.14}$$

where the jump frequency

$$\Sigma = \left\langle \left| \frac{\partial \Gamma}{\partial x_1} \right| \right\rangle = \frac{n_{IB}}{L_1}, \tag{4.15}$$

quantifies the number of alternations n_{IB} between turbulent and non-turbulent fluid (and *vice versa*) per length L_1 along a straight line in the streamwise direction. Figure 9(*a*) shows the jump frequency Σ as a function of the cross-wise coordinate $\hat{x}_3$ at

https://doi.org/10.1017/jfm.2021.399 Published online by Cambridge University Press

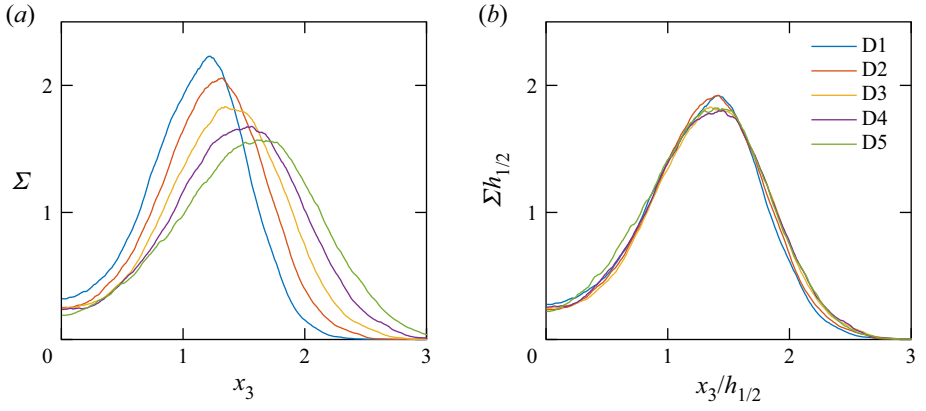

Figure 9. Jump frequency Σ as a function of the cross-wise position x_3 at different times (a) and self-preservation of Σ after normalization with the jet half-width $h_{1/2}$ (b). Data for case D.

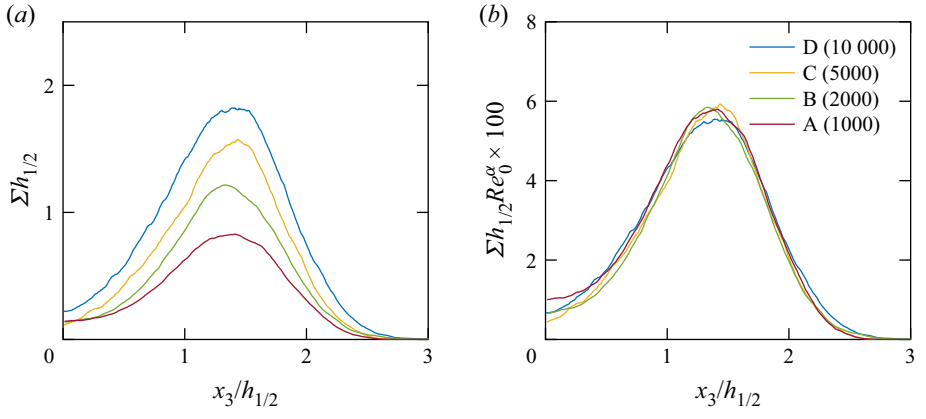

Figure 10. Jump frequency Σ as a function of the cross-wise position $x_3/h_{1/2}$ for different jet Reynolds numbers Re_0 between 1000 and 10 000 (a). The jump frequency becomes approximately independent of Re_0 when rescaled by $h_{1/2}$ and Re_0^{α}, where α is found empirically to be close to -0.4 (b).

different times. It can be observed that Σ is characterized by a single distinct maximum, which identifies the position where the IB is most corrugated. With the spreading of the jet, the maximum decreases and moves outwards in cross-wise direction. After normalization with the half-width $h_{1/2}$, Σ admits a self-preserving shape, see figure 9(b). The consequence of self-preservation is that

$$\frac{n_{IB}}{L_1} \propto h_{1/2}^{-1}, \tag{4.16}$$

which means that the surface of the IB is smoothed as the jet spreads. This observation is consistent with the growth of the characteristic length scales during the self-similar decay of the jet.

Finally, the dependence of the jump frequency Σ on the jet Reynolds Re_0 is of interest. As shown in figure 10, the location of the maximum of Σ remains at approximately $x_3/h_{1/2} = 1.4$ despite a variation of Re_0 by one decade between 1000 and 10 000. However, the value of the maximum clearly increases with the Reynolds number. This increase originates from smaller turbulent length scales that create a more contorted IB at higher

https://doi.org/10.1017/jfm.2021.399 Published online by Cambridge University Press

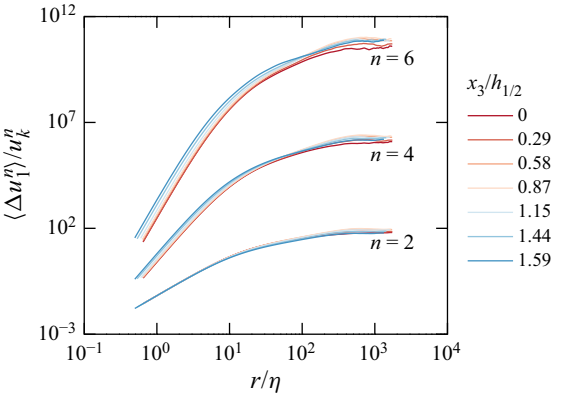

Figure 11. Normalized even-order velocity structure functions up to the sixth order at different cross-wise positions $\hat{x}_3$ from the centreplane (red) up to $\hat{x}_3 = 1.59$ (blue). The structure functions are normalized by the Kolmogorov scales u_k and η. For clarity, the fourth-order structure functions and the sixth-order structure functions are shifted upwards by two and four decades, respectively. Data for case D5.

Reynolds numbers. The shape of the jump frequency $\Sigma h_{1/2}$ becomes approximately Reynolds number independent when rescaled with the jet Reynolds number Re_0^{α}, where α is found empirically to be close to -0.4.

4.3. *Self-similarity of structure functions along the cross-wise direction*

The strong variation of the jump frequency Σ along the cross-wise direction raises the question whether structure functions can admit self-similarity when varying the cross-wise location $\hat{x}_3$ while keeping Re_0 and t constant. Figure 11 shows the normalized second, fourth- and sixth-order velocity structure functions $f_n(\hat{r}, \hat{x}_3)$ at different cross-wise positions between the centreplane and $\hat{x}_3 = 1.59$. The structure functions are normalized by the Kolmogorov scales η and u_k. For the second order, there is reasonable support for self-similarity with respect to $\hat{x}_3$, since an adequate collapse of structure functions can be observed. As expected, the collapse is perfect for the smallest scales, where structure functions obey the classical Kolmogorov scaling $\langle \Delta u_1^2 \rangle / u_k^2 \propto (r/\eta)^2$. At the largest scales, self-similarity still holds with good accuracy despite finite Reynolds number effects.

However, the situation is different for the self-similarity of higher-order structure functions. From figure 11, it is evident that the fourth-order and sixth-order structure functions reveal a non-collapsing and clearly non-self-similar arrangement over the entire range of scales. This finding is in line with the standard paradigm that higher-order statistics are non-universal and highly sensitive to different effects, such as intermittency but also finite Reynolds number effects and the associated coupling to the boundary conditions of the flow. But keeping in mind that higher-order structure functions admit complete self-preservation at the centreplane and in the shear layer at fixed $\hat{x}_3$ (cf. § 3), this finding requires further explanation. The objective of the remainder of the paper is to show that external intermittency plays an important role for the lack of self-similarity of higher-order structure functions.

To visualize the physical mechanism behind the break down of self-similarity, we present in figure 12 the intermittency function Γ and the square of the longitudinal velocity gradient $(\partial u_1/\partial x_1)^2$ at different cross-wise positions $\hat{x}_3$ along a straight line in the streamwise direction x_1. At the centreplane, the jet is fully turbulent and large excursions

https://doi.org/10.1017/jfm.2021.399 Published online by Cambridge University Press

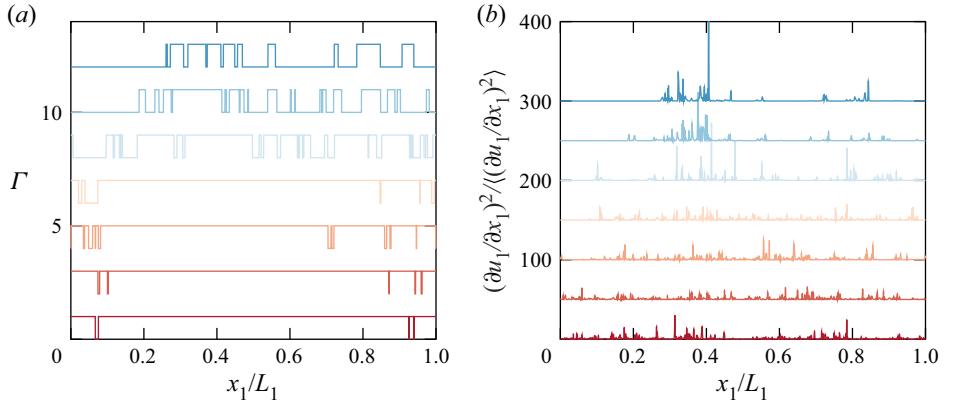

Figure 12. Intermittency function Γ (a) and the square of the longitudinal velocity gradient $(\partial u_1/\partial x_1)^2$ (b) at different cross-wise positions x_3 along a straight line in the streamwise direction x_1. The signals are shifted upwards for clarity. Data for case D5 at different cross-wise positions $\hat{x}_3$ equal to 0.0, 0.29, 0.58, 0.87, 1.15, 1.44 and 1.59 (from bottom to top).

from the mean value of $(\partial u_1/\partial x_1)^2$ occur, which is characteristic of a signal with internal intermittency. These excursions originate from thin, confined layers that are of the order of a few Kolmogorov length scales. Toward the edge of the jet flow, the nature of turbulence changes drastically when external intermittency comes into play. The principal feature of external intermittency is that it imposes external information on the signal. This external information can be quantified statistically at the large scales by the intermittency factor γ (ratio between turbulent and non-turbulent regimes) and at the small scales by the jump frequency Σ (frequency of the alternation between turbulent and non-turbulent regimes). Both quantities depend on the morphology of the IB with the consequence that turbulence is not self-similar along the $\hat{x}_3$ direction. This assertion is now supported by a statistical analysis.

Following Frisch (1995), we define a turbulent signal to be intermittent when it features strong activity only during a fraction of time (or space). To quantify intermittency at different scales, we introduce the relation between structure functions and the p.d.f. of velocity increments $P(\Delta u_1; r, x_3)$,

$$\langle \Delta u_1^n \rangle = \int_{-\infty}^{\infty} \Delta u_1^n P(\Delta u_1; r, x_3)\, \mathrm{d}(\Delta u_1). \tag{4.17}$$

Equation (4.17) highlights that higher-order moments provide information about the far tails of the p.d.f. which makes them a suitable tool for the study of intermittency. The shape of the distribution $P(\Delta u_1; r, x_3)$ can be quantified by the flatness factors

$$F_4^< = \frac{\left\langle \left(\dfrac{\partial u_1}{\partial x_1} \right)^4 \right\rangle}{\left\langle \left(\dfrac{\partial u_1}{\partial x_1} \right)^2 \right\rangle^2}, \tag{4.18}$$

and

$$F_4^> = \frac{\langle u_1^4 \rangle}{\langle u_1^2 \rangle^2}, \tag{4.19}$$

https://doi.org/10.1017/jfm.2021.399 Published online by Cambridge University Press

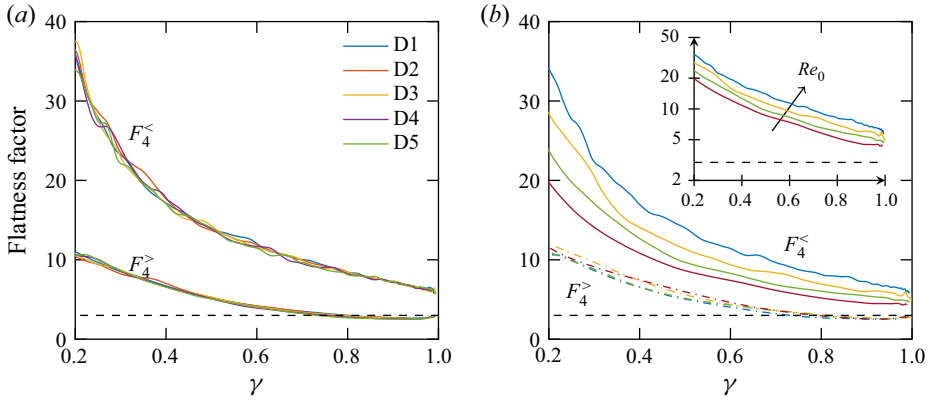

Figure 13. Flatness factor of the velocity gradients $F_4^<$ and the velocity fluctuations $F_4^>$ as a function of the intermittency factor γ at (*a*) different times (cases D1–D5) and (*b*) different jet Reynolds numbers (cases A–D). The black dashed line represents the flatness factor of a Gaussian distribution.

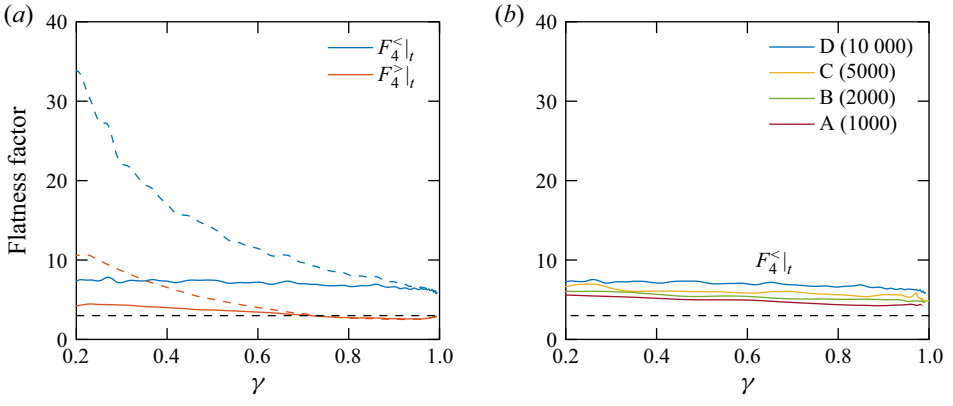

Figure 14. (*a*) Conditional flatness factors $F_4^<|_t$ and $F_4^>|_t$ (solid lines) are approximately independent of the intermittency factor γ. The flatness factors $F_4^<$ and $F_4^>$ (dashed lines) are shown for comparison. (*b*) Dependence of $F_4^<|_t$ on the jet Reynolds number. The black dashed line represents the flatness factor of a Gaussian distribution.

which represent intermittency at the small scales and large scales, respectively. From the dependence of the velocity gradient flatness $F_4^<$ on the external intermittency factor γ, the inter-scale coupling of turbulence can be analysed. Figure 13(*a*) shows that $F_4^<$ increases from a centreplane value close to 6 to a value close to 30 when γ equals 0.2. This dependence clearly demonstrates that external intermittency can have a striking impact on the small scales (represented by $F_4^<$), and that the small scales do not decouple from the large scales (represented by γ). Internal intermittency can be ruled out as the reason for the increase of $F_4^<$ because the turbulent Reynolds number moderately decays toward the edge of the jet. Also, the velocity fluctuation flatness $F_4^>$ increases across the jet from approximately 3 at the centreplane to 10 at $\gamma = 0.2$. This means that the assumption of Gaussianity for the velocity fluctuations is valid in the core but not at the edge of the flow. It is also worth noting that the dependence of the flatness factors $F_4^<$ and $F_4^>$ on γ appears to be self-preserving.

https://doi.org/10.1017/jfm.2021.399 Published online by Cambridge University Press

In figure 13(*b*), we present the effect of the jet Reynolds number Re_0 on the flatness factors. It can be seen that the flatness factor of the velocity gradients $F_4^<$ increases notably with Reynolds number, but its variation with γ is approximately the same for all Reynolds numbers. Based on the concept of scale separation, $F_4^<$ should gradually become less sensitive to external intermittency as the Reynolds number increases. However, this trend is not supported by figure 13(*b*). An explanation for this observation could be the relatively low Reynolds numbers of the simulations at hand for which no sufficient decoupling between small and large scales exists (Mydlarski & Warhaft 1996). Moreover, figure 13(*b*) indicates that the flatness factor of the velocity fluctuations $F_4^>$ depends only weakly on the jet Reynolds number Re_0.

In order to further understand the impact of external intermittency on turbulence, we define conditional flatness factors

$$F_4^<|_t = \frac{\left\langle \Gamma \left(\dfrac{\partial u_1}{\partial x_1} \right)^4 \right\rangle}{\left\langle \Gamma \left(\dfrac{\partial u_1}{\partial x_1} \right)^2 \right\rangle^2}, \tag{4.20}$$

and

$$F_4^>|_t = \frac{\langle \Gamma u_1^4 \rangle}{\langle \Gamma u_1^2 \rangle^2}, \tag{4.21}$$

that consider only the turbulent portion of the jet. Turbulent and non-turbulent regions are distinguished by the intermittency function $\Gamma(\boldsymbol{x})$. Unlike the conventional flatness factors $F_4^<$ and $F_4^>$, figure 14 shows that the conditional flatness factors $F_4^<|_t$ and $F_4^>|_t$ are virtually constant and significantly less sensitive to variations of γ. This finding is valid independently of the jet Reynolds number and originates from strong turbulent transport that leads in a statistical sense to a rapid homogenization of fully turbulent regions. A rapid homogenization of turbulent regions in free shear flows was already speculated by Corrsin & Kistler (1955) and later confirmed by Mellado *et al.* (2009).

Thus far, we have not explained the mechanism behind the inter-scale coupling related to external intermittency. To do this, it is meaningful to study the p.d.f. of the velocity gradients at different cross-wise positions. When the p.d.f. of the velocity gradients is known, the flatness factor $F_4^<$ can be obtained by

$$F_4^< = \int_{-\infty}^{\infty} z^4 \widetilde{P}(z)\,\mathrm{d}z, \tag{4.22}$$

where $z = (\partial u_1/\partial x_1)/\sigma$, $\widetilde{P}(z) = \sigma P(z)$ is the normalized velocity gradient p.d.f., and $\sigma = \langle (\partial u_1/\partial x_1)^2 \rangle^{1/2}$ is the standard deviation. In figure 15(*a*), we present the evolution of $\widetilde{P}(z)$ along the $\hat{x}_3$ direction for case D5. At the centreplane, $\widetilde{P}(z)$ is non-Gaussian and has stretched exponential tails, but principally, the shape is very similar to p.d.f.s known for homogeneous isotropic turbulence (Gotoh, Fukayama & Nakano 2002). From the centreplane to the edge, the tails of $\widetilde{P}(z)$ become increasingly stretched, which is a characteristic footprint of increasing intermittency. In particular, the far tails represent very large velocity gradients that partly stem from the thin interfacial layer between turbulent and non-turbulent fluid (Elsinga & da Silva 2019). At the same time, a distinct peak emerges around $\partial u_1/\partial x_1 = 0$. This peak originates from non-turbulent regions outside of the turbulent envelope where velocity gradients are close to zero. The combination of these effects has two consequences: firstly, the self-similarity of $\widetilde{P}(z)$ is destroyed, and secondly, the flatness factor $F_4^<$ increases toward the edge of the jet. It is now of interest to

https://doi.org/10.1017/jfm.2021.399 Published online by Cambridge University Press

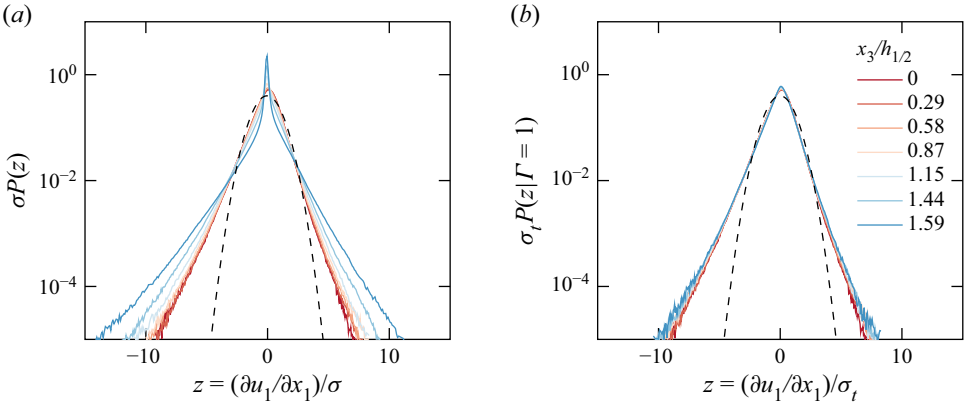

Figure 15. Conventional (*a*) and conditional (*b*) p.d.f. of the velocity gradients $\partial u_1/\partial x_1$ at different cross-wise positions $\hat{x}_3$ as indicated in the legend. The black dashed line indicates a normal distribution. The curves are normalized by the standard deviation $\sigma = \langle(\partial u_1/\partial x_1)^2\rangle^{1/2}$ and the conditional standard deviation $\sigma_t = \langle(\Gamma\partial u_1/\partial x_1)^2\rangle^{1/2}$, respectively. Data for case D5.

compare the results with the conditional p.d.f. that accounts only for the turbulent portion of the flow. The normalized conditional p.d.f. is defined as $\widetilde{P}(z\,|\,\Gamma = 1) = \sigma_t P(z\,|\,\Gamma = 1)$, with $\sigma_t = \langle(\Gamma\partial u_1/\partial x_1)^2\rangle^{1/2}$ being the conditional standard deviation. Figure 15(*b*) reveals that $\widetilde{P}(z|\Gamma = 1)$ recovers self-similarity, with the exception of the very far tails. Based on this comparison, we can conclude that external intermittency is the relevant mechanism that destroys self-similarity along the cross-wise direction.

Finally, we revisit the self-similarity of velocity structure functions. Motivated by the previous discussion, a conditional structure function

$$S_{n,tt} = \langle\Gamma(\boldsymbol{x}+\boldsymbol{e}_1 r)\Gamma(\boldsymbol{x})(u_1(\boldsymbol{x}+\boldsymbol{e}_1 r) - u_1(\boldsymbol{x}))^n\rangle \tag{4.23}$$

is defined for which both ending points are restricted to the turbulent portion of the jet. Sabelnikov *et al.* (2019) defined structure functions in a similar fashion to distinguish in non-premixed flames between burnt and unburnt regions. Figure 16 presents the normalized conditional structure functions $S_{n,tt}$ up to the sixth order at different $\hat{x}_3$ positions. The structure functions are normalized by conditional Kolmogorov scales that account only the turbulent portion of the flow, i.e. $u_{k,t} = (\nu\langle\Gamma\varepsilon\rangle)^{1/4}$ and $\eta_t = (\nu^3/\langle\Gamma\varepsilon\rangle)^{1/4}$. Compared with the conventional structure functions S_n shown in figure 11, the conditional structure functions $S_{n,tt}$ reveal a significantly improved collapse up to a length scale of $r/\eta_t \approx 100$, which corresponds approximately to the middle of the inertial subrange. This observation signifies that turbulent regions smaller than this length scale homogenize rapidly across the jet.

4.4. *Scaling exponents of structure functions*

Let us now examine the connection between the inertial range scaling exponents of structure functions and external intermittency. Kolmogorov (1941*b*) introduced the idea of a scale separation, where under the condition of very large Reynolds numbers an inertial subrange exists, i.e. $\eta \ll r \ll l_t$, in which the pth-order velocity structure function obeys a scaling law, i.e.

$$S_p = \langle|\Delta u_1|^p\rangle \propto r^{\xi_p}, \tag{4.24}$$

https://doi.org/10.1017/jfm.2021.399 Published online by Cambridge University Press

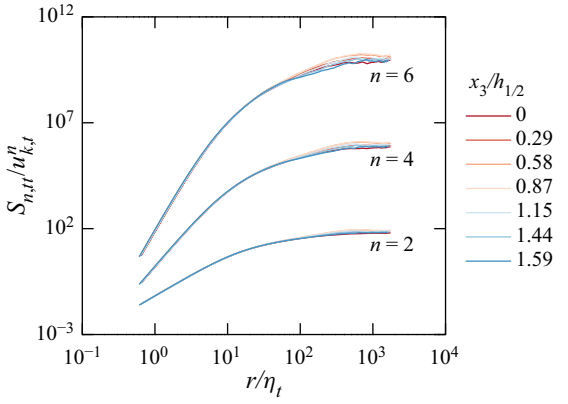

Figure 16. Normalized conditional structure functions $S_{n,tt}$ up to the sixth order at different cross-wise positions $\hat{x}_3$, where both ending points are located inside the turbulent envelope, see (4.23). The structure functions are normalized by the conditional Kolmogorov scales $u_{k,t} = (\nu\langle\Gamma\varepsilon\rangle)^{1/4}$ and $\eta_t = (\nu^3/\langle\Gamma\varepsilon\rangle)^{1/4}$. Similar to figure 11, the fourth-order structure functions and the sixth-order structure functions are shifted upwards by two and four decades, respectively. Data for case D5.

with the scaling exponents ξ_p. Different from Kolmogorov's definition, the absolute value of the velocity increment in (4.24) permits the evaluation of even and uneven moments. The Kolmogorov K41 theory predicts the scaling exponents from dimensional grounds as

$$\xi_p = \frac{p}{3}. \tag{4.25}$$

However, numerous experimental and numerical studies have provided strong evidence for anomalous scaling, which refers to a departure from the analytical scaling law, i.e. $\xi_p < p/3$ for $p > 2$ (Anselmet *et al.* 1984; Maurer, Tabeling & Zocchi 1994; Watanabe & Gotoh 2007; Iyer, Sreenivasan & Yeung 2020). This departure has been explained by internal intermittency, which arises from strong spatio-temporal fluctuations of the energy dissipation rate ε. There is now conclusive evidence that internal intermittency breaks the scale invariance and self-similarity of turbulence (see for example Kolmogorov (1962), Kraichnan (1974) and Lawson *et al.* (2019)). However, an even more pronounced deviation from Kolmogorov's K41 prediction is expected for shear flows that are exposed to external intermittency. Therefore, the dependence of the inertial subrange scaling exponents ξ_p on the cross-wise position $\hat{x}_3$ and the external intermittency factor γ is of interest.

Due to the moderate Reynolds number of the jet flows on hand, a well-developed inertial subrange does not exist (Thiesset, Antonia & Danaila 2013*a*). For this reason, the scaling exponents ξ_p are determined by the so-called extended self-similarity (ESS) framework (Benzi *et al.* 1993, 1995). Instead of evaluating the scaling exponents directly via (4.24), a relative scaling exponent, ξ_p/ξ_2, is obtained by plotting the pth-order structure function against the second-order structure function. Following this procedure, the relative scaling exponents are defined as

$$\frac{\xi_p}{\xi_2} = \frac{\mathrm{d}\log S_p(r; x_3)}{\mathrm{d}\log S_2(r; x_3)}. \tag{4.26}$$

The practical effect of the ESS approach is the increase of the width of the so-called restricted scaling range, which makes it possible to obtain reliable scaling exponents in flows with moderate Reynolds numbers. In general, the scaling exponents of structure functions depend to some degree on the Reynolds number, unless the Reynolds number is

https://doi.org/10.1017/jfm.2021.399 Published online by Cambridge University Press

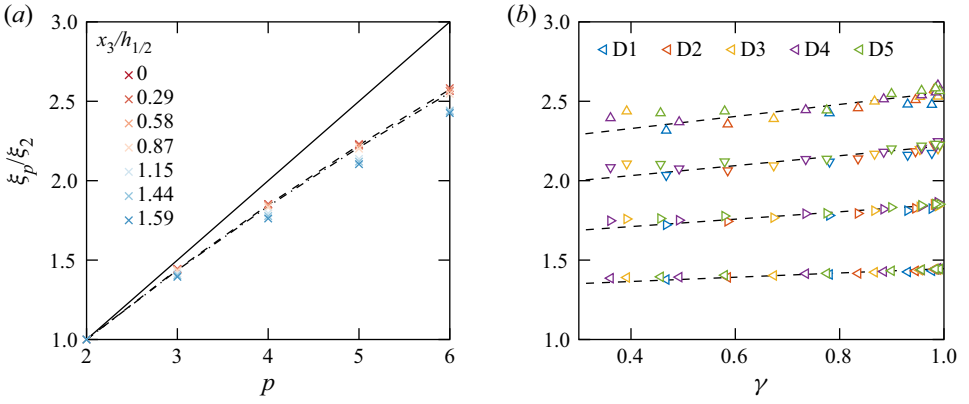

Figure 17. (*a*) Relative scaling exponents ξ_p/ξ_2 obtained by ESS up to the sixth order for different cross-wise positions $\hat{x}_3$ as indicated in the legend for case D5. For comparison Kolmogorov's K41 solution (solid line) as well as the *p*-model (dashed line) are shown. (*b*) Dependence of the relative scaling exponents ξ_p/ξ_2 on the intermittency factor γ at different times and for p increasing from 3 to 6 (from the bottom to the top). The black dashed lines are obtained by a least-square fit and are shown as a visual guide.

very large (Pearson & Antonia 2001; Tang *et al.* 2017). By defining the scaling exponents in (4.26) relative to S_2, this Reynolds number dependence is masked. Here, we take advantage of this feature, because the variation of the Reynolds number across the jet can be ruled out as the reason for variations of the relative scaling exponents.

The scaling exponents ξ_p/ξ_2 obtained by ESS are shown in figure 17(*a*) up to the sixth order for different cross-wise positions. For comparison, we display Kolmogorov's K41 prediction and the *p*-model developed by Meneveau & Sreenivasan (1991), i.e.

$$\xi_p = 1 - \ln_2(0.7^{n/3} + 0.3^{n/3}). \tag{4.27}$$

The *p*-model is based on a multi-fractal approach and is known to be able to predict the inertial subrange scaling exponents of homogeneous isotropic turbulence with very good accuracy (Sreenivasan & Antonia 1997). Figure 17(*a*) shows that the relative scaling exponents at the centreplane depart increasingly from Kolmogorov's K41 prediction with increasing order, but are consistent with the prediction from the *p*-model. Hence, the relative scaling exponents at the centreplane reflect the effect of internal intermittency but are hardly affected by large-scale effects. However, the situation is very different toward the edge of the flow. Figure 17(*a*) shows that the relative scaling exponents ξ_p/ξ_2 fall below the centreplane scaling exponents with increasing distance from the centreplane. This effect becomes more pronounced with increasing order and eventually destroys the self-similarity of higher-order structure functions in the restricted scaling range.

In the next step, we provide evidence that the pronounced anomalous scaling of structure functions can be attributed to external intermittency. Figure 17(*b*) presents the relative scaling exponents ξ_p/ξ_2 as a function of the external intermittency factor γ at different times. As anticipated, the relative scaling exponents decrease with decreasing γ, and the rate of this decrease increases with the order p. From these findings, we can conclude that external fluctuations amplify the break down of small-scale similarity, which in turn manifests itself in a pronounced departure from Kolmogorov's K41 prediction. Interestingly enough, the variation of the scaling exponents ξ_p/ξ_2 with γ is approximately self-preserving.

These observations mandate a further explanation. Watanabe *et al.* (2019) showed that the dynamics of the energy cascade at the TNTI is very complex and demonstrated that

https://doi.org/10.1017/jfm.2021.399 Published online by Cambridge University Press

turbulence at the TNTI is very far from equilibrium. The scale-by-scale budget analysis in the vicinity of the TNTI by Watanabe, da Silva & Nagata (2020) and Zhou & Vassilicos (2020) further revealed that the direction of the inter-scale transport depends on the local kinematics of the velocity field at the TNTI. In particular, Zhou & Vassilicos (2020) showed that the most intense inter-scale transport occurs when the TNTI is furthest away from the centre of the jet. These spatial variations of the inter-scale transport may contribute to the observed amplified departure of the scaling exponents from the K41 prediction.

4.5. *The correlation of the dissipation rate*

Since the famous remark by Landau & Lifshitz (1963), it is known that the intermittent fluctuations of the dissipation rate play an important role in the failure of analytical scaling relations of higher-order structure functions. Following Landau's remark, Obukhov (1962) proposed to replace the mean dissipation in Kolmogorov's K41 scaling theory by a coarse-grained dissipation ε_r that is spatially averaged over a sphere of radius r. In anisotropic turbulence, ε_r is usually defined by a one-dimensional surrogate as

$$\varepsilon_r = \frac{1}{r}\int_{\boldsymbol{x}}^{\boldsymbol{x}+r\boldsymbol{e}_1} \varepsilon(\widetilde{\boldsymbol{x}})\,\mathrm{d}\widetilde{\boldsymbol{x}}. \tag{4.28}$$

To address Landau's remark, Kolmogorov (1962) presented the so-called refined similarity hypothesis, which is a quantitative theory that accounts for intermittency. Provided that an inertial subrange exists, the central assumption of this theory is the scaling of $\langle\varepsilon_r^2\rangle$, i.e.

$$\langle\varepsilon_r^2\rangle \propto \langle\varepsilon^2\rangle(r/l_t)^{-\mu} \tag{4.29}$$

that defines the intermittency exponent μ. Most experiments reported values for μ between 0.15 and 0.25 (Nelkin 1994). Note that in the absence of intermittency, the exponent μ tends to zero. By making the assumption that ε_r obeys a log-normal distribution, Kolmogorov (1962) linked the scaling exponent of structure function to the intermittency exponent, i.e. $\xi_p = \mu p(3-p)/18$. For $p < 10$, Kolmogorov's log-normal assumption provides satisfactory agreement with experiments (Frisch 1995).

Despite the relatively low Reynolds number of the flow at hand, it is instructive to study how $\langle\varepsilon_r^2\rangle$ depends on the cross-wise position $\hat{x}_3$. Nelkin (1994) showed that the two-point correlation of the dissipation rate is related to $\langle\varepsilon_r^2\rangle$, i.e.

$$\mathcal{R}_\varepsilon(r, x_3) = \langle\varepsilon(\boldsymbol{x})\varepsilon(\boldsymbol{x}+r\boldsymbol{e}_1)\rangle = \frac{1}{2}\frac{\mathrm{d}^2\langle\varepsilon_r^2\rangle}{\mathrm{d}r^2}, \tag{4.30}$$

which follows from (4.28) and homogeneity in the streamwise direction. In what follows, we focus on the two-point correlation function, because it allows us to define a conditional average similar to (4.23). The two-point correlation function $\mathcal{R}_\varepsilon$ is presented in figure 18(*a*) for different cross-wise positions $\hat{x}_3$ for case D5. Normalization with $\langle\varepsilon^2\rangle$ yields a perfect collapse of the correlation functions in the dissipative range. For larger scales at approximately $r/\eta > 10$, the different correlation functions begin to depart and approach a plateau in the large-scale limit, whose value clearly depends on $\hat{x}_3$. The consequence of this observation is the fact that there is a range of scales between $10 < r/\eta < 100$, for which the slope of $\mathcal{R}_\varepsilon$ becomes significantly steeper from the centre to the edge. In other words, the intermittency exponent μ increases from the centre toward the edge of the jet. This observation is consistent with the amplified anomalous scaling of structure functions shown in figure 17.

https://doi.org/10.1017/jfm.2021.399 Published online by Cambridge University Press

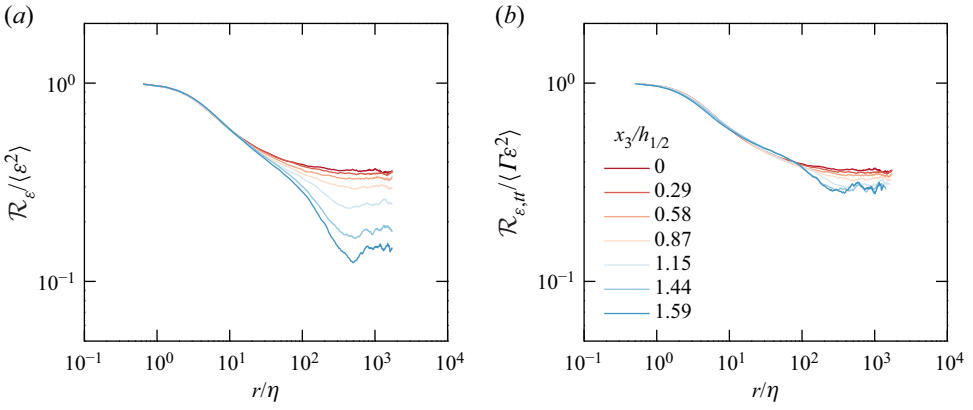

Figure 18. Normalized correlation function of the dissipation $\mathcal{R}_\varepsilon = \langle\varepsilon(\boldsymbol{x})\varepsilon(\boldsymbol{x}+r\boldsymbol{e}_1)\rangle$ (*a*) and normalized conditional correlation function $\mathcal{R}_{\varepsilon,tt} = \langle\Gamma(\boldsymbol{x})\Gamma(\boldsymbol{x}+r\boldsymbol{e}_1)\varepsilon(\boldsymbol{x})\varepsilon(\boldsymbol{x}+r\boldsymbol{e}_1)\rangle$ (*b*) for different cross-wise positions $\hat{x}_3$. Data are shown for case D5.

In order to study the effect of external intermittency, we define the conditional correlation function of the dissipation rate as

$$\mathcal{R}_{\varepsilon,tt}(r, x_3) = \langle\Gamma(\boldsymbol{x})\Gamma(\boldsymbol{x}+r\boldsymbol{e}_1)\varepsilon(\boldsymbol{x})\varepsilon(\boldsymbol{x}+r\boldsymbol{e}_1)\rangle, \tag{4.31}$$

where, similar to the conditional structure function defined by (4.23), both points $\boldsymbol{x}+r\boldsymbol{e}_1$ and $\boldsymbol{x}$ are restricted to the turbulent portion of the jet. The conditional correlation function $\mathcal{R}_{\varepsilon,tt}$ is shown in figure 18(*b*) and reveals, compared with $\mathcal{R}_\varepsilon$, an improved collapse. In particular, the slope in the range $10 < r/\eta < 100$ hardly depends on the cross-wise position. This result is consistent with the collapse of the conditional structure function $S_{n,tt}/u_{k,t}^n$ shown in figure 16.

5. Summary and discussion

After decades of research, the concept of self-similarity of structure functions in turbulent jet flows is still considered very elusive. The reason is the existence of strong spatio-temporal fluctuations that occur over a wide range of different scales and usually invalidate self-similarity approaches. In turbulent jet flows, these fluctuations originate not only from internal intermittency but also from external intermittency. Specifically, it is unclear if and how internal and external intermittency are coupled.

In the first step, we demonstrated that velocity structure functions satisfy complete self-preservation at the centre and in the shear layer of jet flows. We showed that self-preservation is not limited to low-order structure functions, but also valid for higher orders. By studying asymptotic solutions of structure functions, we derived necessary conditions for self-preservation in the small-scale and large-scale limits. We showed that a constant, but not necessarily very high Reynolds number is required for complete self-preservation. The analysis also revealed that isotropy is not required for complete self-preservation to be valid. Instead, the analysis showed that any anisotropy that is present in the flow must persist indefinitely.

In the next step, we studied the self-similarity of structure functions at different cross-wise positions. The edge of a jet is characterized by the IB, which in turn is associated with the phenomenon of external intermittency. For the study of external intermittency, we defined the intermittency structure function, which quantifies the morphology of the IB at different scales.

https://doi.org/10.1017/jfm.2021.399 Published online by Cambridge University Press

The analysis revealed that Kolmogorov's K41 theory provides suitable self-similarity scales for second-order velocity structure functions at any cross-wise position, despite the presence of finite Reynolds number effects such as shear, inhomogeneity or external intermittency. However, the analysis also demonstrated that external intermittency has a similarity-breaking effect on higher-order structure functions. The similarity-breaking effect becomes more pronounced with increasing order and has its origin in a combination of the occurrence of strong velocity gradients and the alternating flow structure of turbulent and non-turbulent fluid.

Further evidence for the self-similarity-breaking effect of external intermittency was provided by representing statistics as a function of the intermittency factor γ. An important result is the increase of the flatness factor of the velocity gradients as the impact of external intermittency increases. This finding clearly indicates that the large scales (represented by the external intermittency factor) are coupled to the small scales (represented by the velocity gradient flatness) of the flow. Similar conclusions were drawn for the inertial range scaling exponents of structure functions, which exhibit a pronounced departure from Kolmogorov's K41 prediction toward the edge of the flow. In particular, the data provide no evidence that the effect of external intermittency on small-scale turbulence weakens as the Reynolds number increases.

The reported results are significant for mixing models and combustion models, which require a characteristic turbulence time scale. This time scale is usually built on dimensional grounds with the mean turbulent energy $\langle k \rangle$ and the mean energy dissipation rate $\langle \varepsilon \rangle$. In turbulent flows that are subject to strong intermittency, such a time scale may not be appropriate. Instead, the characteristic time scale should account for the increased intermittency toward the edge of the flow. Such a time scale can be built for example from the higher-order moments of the velocity fluctuations $\langle k^n \rangle$ and the energy dissipation rate $\langle \varepsilon^n \rangle$. By analysing structure functions across the jet, we demonstrated that higher-order statistics conditioned on fully turbulent regions inside the turbulent envelope are largely independent of external intermittency and recover self-similarity at small and intermediate scales. As zonal models, for example based on gradient trajectories (Mellado *et al.* 2009; Gauding *et al.* 2017; Denker *et al.* 2020; Gauding *et al.* 2021), have recently gained relevance for mixing and combustion models, this result has a direct application.

Acknowledgements. The authors gratefully acknowledge the computing time granted through the Gauss-Centre for Supercomputing (GCS) and Jülich Aachen Research Alliance (JARA) on the supercomputers JUQUEEN and JURECA at Juelich Supercomputing Centre (Germany) under grants HFG00, jhpc55 and TURBULENCESL. Furthermore, computing time granted on MYRIA by CRIANN is gratefully acknowledged. The authors are very grateful for helpful discussions with Dr F. Thiesset.

Funding. Financial support was provided by EMCO2RE. L.D. thanks for support from ANR under grant QUTE-HPC.

Declaration of interests. The authors report no conflict of interest.

Appendix A. Statistical convergence of higher-order statistics and suitability of the threshold criterion for the detection of the IB

Higher-order moments are strongly influenced by rare but very intense events. For this reason, the statistical convergence is demanding and requires averaging over a sufficient large ensemble. Following Meneveau & Marusic (2013) and de Silva *et al.* (2017), we verify the convergence of the higher-order moments by the pre-multiplied p.d.f.s of the energy dissipation rate and the turbulent energy. The non-dimensional moments of the energy dissipation rate $\langle \varepsilon^n \rangle / \langle \varepsilon \rangle^n$ can be obtained by integrating the pre-multiplied p.d.f.,

https://doi.org/10.1017/jfm.2021.399 Published online by Cambridge University Press

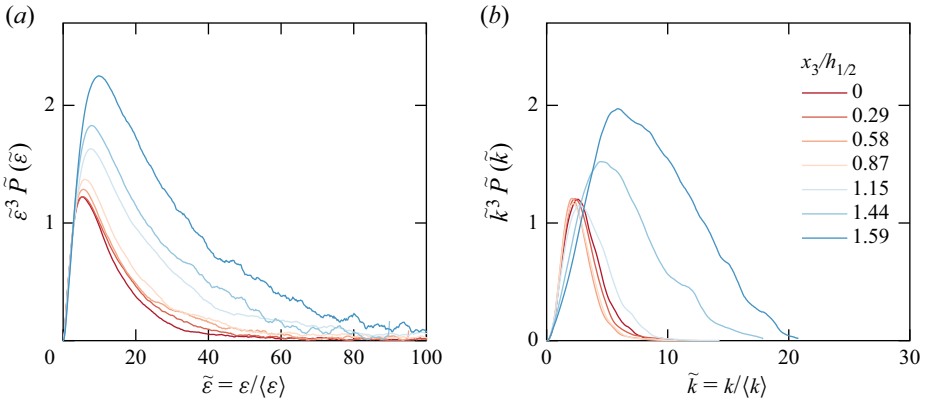

Figure 19. (*a*) Pre-multiplied p.d.f. of the energy dissipation rate to obtain the non-dimensional third-order moment, defined as $\langle\varepsilon^3\rangle/\langle\varepsilon\rangle^3 = \int_0^\infty \tilde{\varepsilon}^3\widetilde{P}(\tilde{\varepsilon})\,\mathrm{d}\tilde{\varepsilon}$, with $\widetilde{P}(\tilde{\varepsilon}) = \langle\varepsilon\rangle P(\varepsilon/\langle\varepsilon\rangle)$. (*b*) The pre-multiplied p.d.f. of the turbulent energy k is defined in a similar fashion. The curves are shown for different cross-wise positions $\hat{x}_3$ as indicated in the legend. Data for case D5.

i.e.

$$\frac{\langle\varepsilon^n\rangle}{\langle\varepsilon\rangle^n} = \int_0^\infty \tilde{\varepsilon}^n\widetilde{P}(\tilde{\varepsilon})\,\mathrm{d}\tilde{\varepsilon}, \tag{A1}$$

with the normalized p.d.f. being defined as $\widetilde{P}(\tilde{\varepsilon}) = \langle\varepsilon\rangle P(\varepsilon/\langle\varepsilon\rangle)$. The integral quantity of (A1) is shown for the third order in figure 19(*a*) for different cross-wise positions $\hat{x}_3$. It can be seen that the integral under the curve is well approximated by the data available, indicating satisfactory statistical convergence of the third-order moment (note that the third-order moment of the dissipation rate is related to the sixth-order moment of structure functions in the small-scale limit). Statistical convergence is more challenging toward the edge of the jet due to external intermittency, which is clearly visible in the pre-multiplied p.d.f. by large excursions from the mean. It is remarkable that ε attains for the most outward position $\hat{x}_3 = 1.59$ values as large as 100 times the mean value $\langle\varepsilon\rangle$.

To examine the statistical convergence at the large scales, we define in a similar fashion the non-dimensional moments of the turbulent energy k, i.e.

$$\frac{\langle k^n\rangle}{\langle k\rangle^n} = \int_0^\infty \tilde{k}^n\widetilde{P}(\tilde{k})\,\mathrm{d}\tilde{k}, \tag{A2}$$

with $\widetilde{P}(\tilde{k}) = \langle k\rangle P(k/\langle k\rangle)$. Similarly, the integral quantity of (A2) is shown for the third order in figure 19(*b*) for different cross-wise positions $\hat{x}_3$. Satisfactory statistical convergence of the pre-multiplied p.d.f. can be observed.

Structure functions are scale-sensitive statistics and especially for higher orders, their convergence needs to be carefully examined. The situation is even more challenging for conditional structure functions $S_{n,tt}$, where the number of events that contribute to the ensemble average decreases continuously from the centre to the edge of the jet (see (4.23)). We verify the statistical convergence by comparing structure functions that are computed over a single (x_1, x_2)-plane with structure functions that are computed over two (x_1, x_2)-planes by exploiting symmetry with respect to the midplane. Figure 20(*a*) shows the conditional structure functions $S_{n,tt}$ up to the sixth order for $\hat{x}_3 = 1.59$. Overall, a satisfactory statistical quality can be observed. Small differences are limited to the largest scales.

https://doi.org/10.1017/jfm.2021.399 Published online by Cambridge University Press

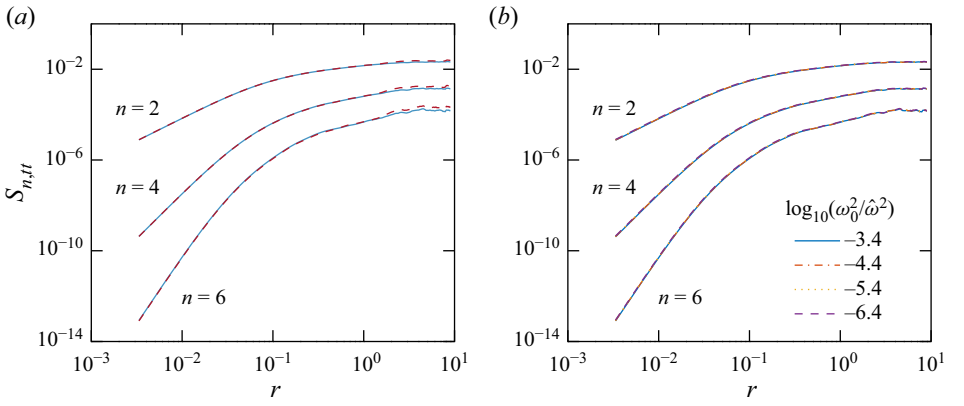

Figure 20. (*a*) Illustration of the statistical quality of conditional structure functions $S_{n,tt}$ up to the sixth order at the position $\hat{x}_3 = 1.59$ for case D5. The solid blue lines represent an ensemble average that exploits symmetry with respect to the midplane, while the dashed red lines represent an ensemble average that is computed over a single (x_1, x_2) plane. (*b*) Dependence of the conditional structure functions $S_{n,tt}$ on the value of the threshold $\log_{10}(\omega_0^2/\hat{\omega}^2)$ that determines the IB at the position $\hat{x}_3 = 1.59$ for case D5 (see § 4.1). For reasons of comparability, the structure functions are not normalized.

Furthermore, it is necessary to examine how the conditional structure functions $S_{n,tt}$ depend on the threshold of the enstrophy that determines the position of the IB. Figure 20(*b*) shows $S_{n,tt}$ up to the sixth order at the position $\hat{x}_3 = 1.59$ for different thresholds $\log_{10}(\omega_0^2/\hat{\omega}^2)$ between -6.4 and -3.4 (see § 4.1). It can be observed that the conditional structure functions $S_{n,tt}$ hardly depend on the threshold, despite a variation of the threshold value by three orders of magnitude. Consequently, the results presented are essentially independent of the chosen threshold value.

Appendix B. Self-similarity analysis of the temporally evolving planar jet

We apply the self-similarity theory of Townsend (1949) to the temporally evolving planar jet flow. The starting point is the Reynolds-averaged streamwise momentum balance, formulated at the centreplane

$$\frac{\partial \langle U_1 \rangle}{\partial t} = -\frac{\partial}{\partial x_3}\langle u_1 u_3 \rangle + \nu \frac{\partial^2 \langle U_1 \rangle}{\partial x_3^2}. \tag{B1}$$

Self-preservation of the independent variables of (B1) is assumed, which leads to the following functional relations:

$$\langle U_1 \rangle = U_{ref}(t) f(\hat{x}_3) \quad \text{and} \quad \langle u_1 u_3 \rangle = U_{ref}^2(t) g(\hat{x}_3), \tag{B2a,b}$$

where U_{ref} is a reference velocity scale that depends only on time t, while g and f are non-dimensional functions that depend on the normalized transverse coordinate $\hat{x}_3 = x_3/L_{ref}$, where L_{ref} is a reference length scale.

Using (B2*a*,*b*) in (B1) gives, after rearranging,

$$\left[\frac{L_{ref}^2}{\nu U_{ref}}\frac{\mathrm{d}U_{ref}}{\mathrm{d}\hat{t}}\right] f(\hat{x}_3) - \left[\frac{L_{ref}}{\nu}\frac{\mathrm{d}L_{ref}}{\mathrm{d}\hat{t}}\right]\hat{x}_3 f'(\hat{x}_3) = -\left[\frac{U_{ref}L_{ref}}{\nu}\right] g(\hat{x}_3) + f''(\hat{x}_3), \tag{B3}$$

https://doi.org/10.1017/jfm.2021.399 Published online by Cambridge University Press

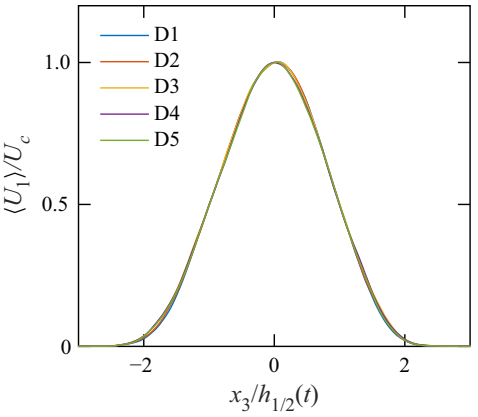

Figure 21. Mean streamwise velocity profile normalized with the mean centreplane velocity U_c and the jet half-width $h_{1/2}$ at different times (D1–D5) indicated in figure 1.

where the prime denotes derivatives with respect to $\hat{x}_3$ and $\hat{t} = t/t_{ref}$. The reference time $t_{ref} = H_0/U_0$ is built with the initial jet thickness H_0 and the initial jet centreplane velocity U_0. Self-preservation requires that the prefactors in the square brackets of (B3) are constant, i.e.

$$\frac{L_{ref}^2}{\nu U_{ref}} \frac{\mathrm{d}U_{ref}}{\mathrm{d}t} = c_1, \tag{B4}$$

$$\frac{L_{ref}}{\nu} \frac{\mathrm{d}L_{ref}}{\mathrm{d}t} = c_2, \tag{B5}$$

$$\frac{U_{ref} L_{ref}}{\nu} = c_3. \tag{B6}$$

The constants c_1, c_2 and c_3 are invariant with time, but may still depend on the initial conditions. This also signifies that different independent self-similarity solutions may exist for different Reynolds numbers. Notwithstanding, the opportunity created by this development lies in the fact that we can analyse dynamical constraints of the governing equations that follow from self-preservation. Specifically, we demonstrate in the following that the temporal evolution of the characteristic velocity and time scales can be determined unambiguously under the condition of self-preservation.

Integrating (B5) reveals the time dependence of the characteristic length scale L_{ref} to be

$$\left(\frac{L_{ref}}{L_0} \right)^2 = \frac{2c_2}{Re_0} (\hat{t} - \hat{t}_0), \tag{B7}$$

where $\hat{t}_0$ is the virtual origin in time. Integrating (B4) gives the temporal evolution of the characteristic velocity, i.e.

$$\frac{U_{ref}}{U_0} = A_u (\hat{t} - \hat{t}_0)^n, \tag{B8}$$

where the scaling exponent equals $n = c_1/(2c_2)$ and A_u is a non-dimensional constant. Self-preservation of the mean velocity profile $\langle U_1 \rangle$ in conjunction with continuity dictates

https://doi.org/10.1017/jfm.2021.399 Published online by Cambridge University Press

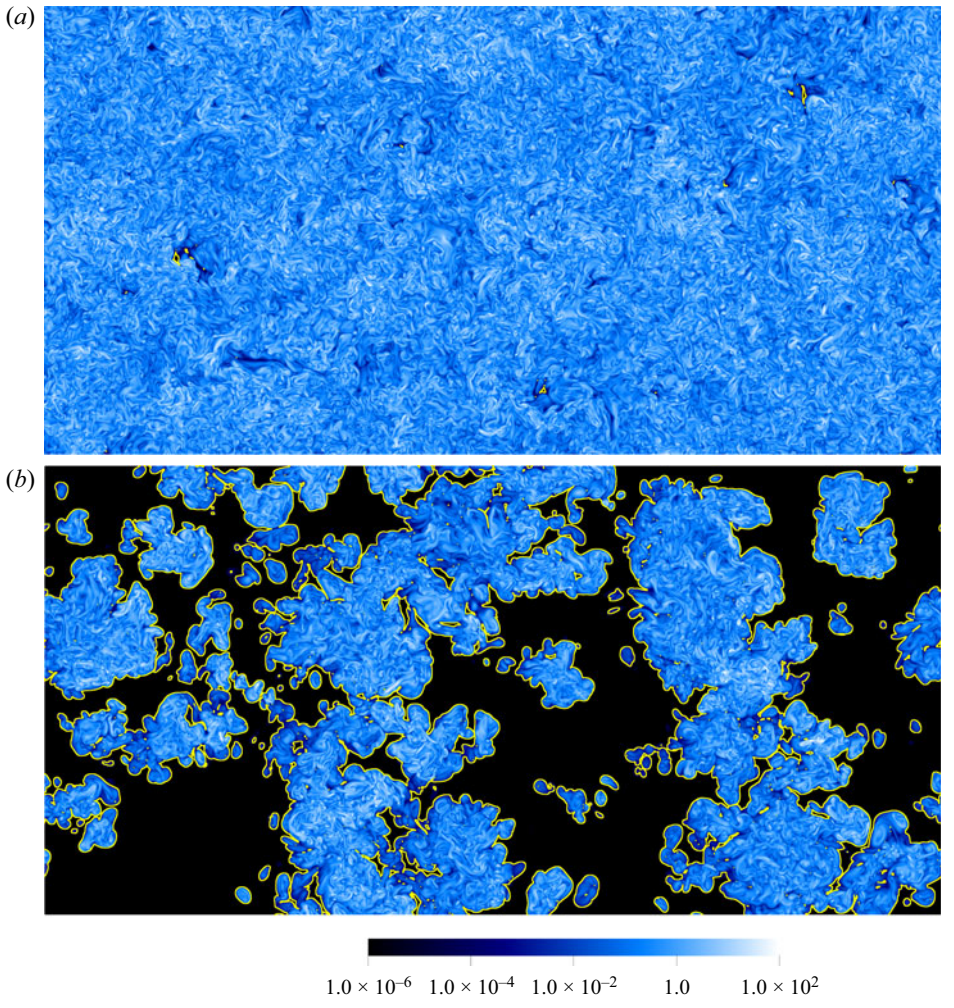

Figure 22. Two-dimensional (x_1, x_2)-plane of the normalized enstrophy $\omega^2/\hat{\omega}^2$ at the centreplane (*a*) and at $\hat{x}_3 = 1.59$ (*b*) for case D5. The colour map is scaled logarithmically and increases in the order black (lowest value), blue, white (highest value). The yellow contour lines indicate the IB, defined by the enstrophy criterion as $\log_{10}(\omega_0^2/\hat{\omega}^2) = -3.4$. Note that 50 % of the computational domain is shown.

that the scaling exponent n equals $-1/2$. Using (B7) and (B8) in (B6) gives

$$c_3 = \frac{U_{ref} L_{ref}}{\nu} = \text{const.}, \tag{B9}$$

which implies that the jet Reynolds number

$$Re_L = \frac{U_{ref} L_{ref}}{\nu} \tag{B10}$$

must stay constant for self-preservation to hold.

At this stage of the analysis the reference scales U_{ref} and L_{ref} have not yet been specified. Figure 21 reveals that the mean velocity profiles $\langle U_1 \rangle$ admit self-preservation after normalization with the centreplane velocity U_c and the jet half-width $h_{1/2}$. Thus, U_c

https://doi.org/10.1017/jfm.2021.399 Published online by Cambridge University Press

and $h_{1/2}$ constitute a possible set of self-similarity variables. However, in § 3.2 we show that other sets of length and velocity scales are equally suitable as reference scales.

Appendix C. Visualization of internal and external intermittency

In this section, we present the normalized enstrophy field $\omega^2/\hat{\omega}^2$ in two different (x_1, x_2)-planes to visualize the effect of intermittency, cf. figure 22. At the centreplane, the flow is fully turbulent and a high level of internal intermittency is visible. At the edge of the flow at $\hat{x}_3 = 1.59$, the structure of the enstrophy field is very different and external intermittency is represented by the alternation between non-turbulent regions in black and highly turbulent regions in blue. Both regions are separated by the IB, which is displayed in yellow. The ratio between the blue area and the black area equals the intermittency factor γ. It is clearly visible that the intermittency factor is close to unity at the centreplane, while it is significantly lower than unity at $\hat{x}_3 = 1.59$.

References

Anselmet, F., Gagne, Y., Hopfinger, E. & Antonia, R. 1984 High-order velocity structure functions in turbulent shear flows. *J. Fluid Mech.* **140**, 63–89.

Antonia, R.A., Smalley, R., Zhou, T., Anselmet, F. & Danaila, L. 2003 Similarity of energy structure functions in decaying homogeneous isotropic turbulence. *J. Fluid Mech.* **487**, 245–269.

Benzi, R., Ciliberto, S., Baudet, C. & Chavarria, G.R. 1995 On the scaling of three-dimensional homogeneous and isotropic turbulence. *Physica D* **80** (4), 385–398.

Benzi, R., Ciliberto, S., Tripiccione, R., Baudet, C., Massaioli, F. & Succi, S. 1993 Extended self-similarity in turbulent flows. *Phys. Rev.* A **48** (1), R29–R32.

Bisset, D.K., Hunt, J.C. & Rogers, M.M. 2002 The turbulent/non-turbulent interface bounding a far wake. *J. Fluid Mech.* **451**, 383–410.

Bode, M., Gauding, M., Lian, Z., Denker, D., Davidovic, M., Kleinheinz, K., Jitsev, J. & Pitsch, H. 2021 Using physics-informed enhanced super-resolution generative adversarial networks for subfilter modeling in turbulent reactive flows. *Proc. Combust. Inst.* **38** (2), 2617–2625.

Boschung, J., Hennig, F., Gauding, M., Pitsch, H. & Peters, N. 2016 Generalised higher-order Kolmogorov scales. *J. Fluid Mech.* **794**, 233–251.

Casciola, C., Gualtieri, P., Benzi, R. & Piva, R. 2003 Scale-by-scale budget and similarity laws for shear turbulence. *J. Fluid Mech.* **476**, 105–114.

Chien, C.-C., Blum, D.B. & Voth, G.A. 2013 Effects of fluctuating energy input on the small scales in turbulence. *J. Fluid Mech.* **737**, 527–551.

Corrsin, S. & Kistler, A.L. 1955 Free-stream boundaries of turbulent flows. *NACA Tech. Rep.* 1244.

Debye, P., Anderson, H.Jr. & Brumberger, H. 1957 Scattering by an inhomogeneous solid. II. The correlation function and its application. *J. Appl. Phys.* **28** (6), 679–683.

Debye, P. & Bueche, A. 1949 Scattering by an inhomogeneous solid. *J. Appl. Phys.* **20** (6), 518–525.

Denker, D., Attili, A., Boschung, J., Hennig, F., Gauding, M., Bode, M. & Pitsch, H. 2020 Dissipation element analysis of non-premixed jet flames. *J. Fluid Mech.* **905**, A4.

Djenidi, L., Lefeuvre, N., Kamruzzaman, M. & Antonia, R. 2017 On the normalized dissipation parameter c_ε in decaying turbulence. *J. Fluid Mech.* **817**, 61–79.

Elsinga, G. & da Silva, C. 2019 How the turbulent/non-turbulent interface is different from internal turbulence. *J. Fluid Mech.* **866**, 216–238.

Erlebacher, G., Hussaini, M., Kreiss, H. & Sarkar, S. 1990 The analysis and simulation of compressible turbulence. *Theor. Comput. Fluid Dyn.* **2** (2), 73–95.

Fitzhugh, R. 1983 Statistical properties of the asymmetric random telegraph signal, with applications to single-channel analysis. *Math. Biosci.* **64** (1), 75–89.

Frisch, U. 1995 *Turbulence - The legacy of A.N. Kolmogorov*. Cambridge University Press.

Gauding, M., Bode, M., Denker, D., Brahami, Y., Danaila, L. & Varea, E. 2021 On the combined effect of internal and external intermittency in turbulent non-premixed jet flames. *Proc. Combust. Inst.* **38** (2), 2767–2774.

Gauding, M., Dietzsch, F., Goebbert, J.H., Thévenin, D., Abdelsamie, A. & Hasse, C. 2017 Dissipation element analysis of a turbulent non-premixed jet flame. *Phys. Fluids* **29** (8), 085103.

https://doi.org/10.1017/jfm.2021.399 Published online by Cambridge University Press

GAUDING, M., WANG, L., GOEBBERT, J.H., BODE, M., DANAILA, L. & VAREA, E. 2019 On the self-similarity of line segments in decaying homogeneous isotropic turbulence. *Comput. Fluids* **180**, 206–217.

GAUDING, M., WICK, A., PITSCH, H. & PETERS, N. 2014 Generalised scale-by-scale energy-budget equations and large-eddy simulations of anisotropic scalar turbulence at various Schmidt numbers. *J. Turbul.* **15** (12), 857–882.

GEORGE, W.K. 1992 Self-preservation of temperature fluctuations in isotropic turbulence. In *Studies in Turbulence*, pp. 514–528. Springer.

GEORGE, W.K. 2009 Is there an asymptotic effect of initial and upstream conditions on turbulence? In *ASME 2008 Fluids Engineering Division Summer Meeting collocated with the Heat Transfer, Energy Sustainability, and 3rd Energy Nanotechnology Conferences*, pp. 647–672. American Society of Mechanical Engineers Digital Collection.

GONZALEZ, M. & FALL, A. 1998 The approach to self-preservation of scalar fluctuations decay in isotropic turbulence. *Phys. Fluids* **10** (3), 654–661.

GOTOH, T., FUKAYAMA, D. & NAKANO, T. 2002 Velocity field statistics in homogeneous steady turbulence obtained using a high-resolution direct numerical simulation. *Phys. Fluids* **14** (3), 1065–1081.

HOLZNER, M., LIBERZON, A., NIKITIN, N., LÜTHI, B., KINZELBACH, W. & TSINOBER, A. 2008 A lagrangian investigation of the small-scale features of turbulent entrainment through particle tracking and direct numerical simulation. *J. Fluid Mech.* **598**, 465–475.

HUNGER, F., GAUDING, M. & HASSE, C. 2016 On the impact of the turbulent/non-turbulent interface on differential diffusion in a turbulent jet flow. *J. Fluid Mech.* **802**, R5.

IYER, K.P., SREENIVASAN, K.R. & YEUNG, P. 2020 Scaling exponents saturate in three-dimensional isotropic turbulence. *Phys. Rev. Fluids* **5** (5), 054605.

VON KÁRMÁN, T. & HOWARTH, L. 1938 On the statistical theory of isotropic turbulence. *Proc. R. Soc. Lond.* A **164** (917), 192–215.

KOLMOGOROV, A.N. 1941*a* Dissipation of energy in locally isotropic turbulence. *Dokl. Akad. Nauk SSSR* **32**, 16–18.

KOLMOGOROV, A.N. 1941*b* The local structure of turbulence in incompressible viscous fluid for very large Reynolds numbers. *Dokl. Akad. Nauk SSSR* **30**, 299–303.

KOLMOGOROV, A.N. 1962 A refinement of previous hypotheses concerning the local structure of turbulence in a viscous incompressible fluid at high Reynolds number. *J. Fluid Mech.* **13** (1), 82–85.

KRAICHNAN, R.H. 1974 On Kolmogorov's inertial-range theories. *J. Fluid Mech.* **62** (2), 305–330.

KRUG, D., CHUNG, D., PHILIP, J. & MARUSIC, I. 2017*a* Global and local aspects of entrainment in temporal plumes. *J. Fluid Mech.* **812**, 222–250.

KRUG, D., HOLZNER, M., MARUSIC, I. & VAN REEUWIJK, M. 2017*b* Fractal scaling of the turbulence interface in gravity currents. *J. Fluid Mech.* **820**, R3.

KUZNETSOV, V., PRASKOVSKY, A. & SABELNIKOV, V. 1992 Fine-scale turbulence structure of intermittent hear flows. *J. Fluid Mech.* **243**, 595–622.

LANDAU, L. & LIFSHITZ, E. 1963 Fluid mechanics.

LAWSON, J.M., BODENSCHATZ, E., KNUTSEN, A.N., DAWSON, J.R. & WORTH, N.A. 2019 Direct assessment of Kolmogorov's first refined similarity hypothesis. *Phys. Rev. Fluids* **4** (2), 022601.

LELE, S.K. 1992 Compact finite difference schemes with spectral-like resolution. *J. Comput. Phys.* **103** (1), 16–42.

MAURER, J., TABELING, P. & ZOCCHI, G. 1994 Statistics of turbulence between two counterrotating disks in low-temperature helium gas. *Europhys. Lett.* **26** (1), 31.

MELDI, M. & SAGAUT, P. 2013 Further insights into self-similarity and self-preservation in freely decaying isotropic turbulence. *J. Turbul.* **14** (8), 24–53.

MELLADO, J.P. & ANSORGE, C. 2012 Factorization of the fourier transform of the pressure-poisson equation using finite differences in colocated grids. *Z. Angew. Math. Mech.* **92** (5), 380–392.

MELLADO, J.P., STEVENS, B., SCHMIDT, H. & PETERS, N. 2010 Two-fluid formulation of the cloud-top mixing layer for direct numerical simulation. *Theor. Comput. Fluid Dyn.* **24** (6), 511–536.

MELLADO, J.P., WANG, L. & PETERS, N. 2009 Gradient trajectory analysis of a scalar field with external intermittency. *J. Fluid Mech.* **626**, 333–365.

MENEVEAU, C. & MARUSIC, I. 2013 Generalized logarithmic law for high-order moments in turbulent boundary layers. *J. Fluid Mech.* **719**, R1.

MENEVEAU, C. & SREENIVASAN, K. 1991 The multifractal nature of turbulent energy dissipation. *J. Fluid Mech.* **224**, 429–484.

MI, J. & ANTONIA, R. 2001 Effect of large-scale intermittency and mean shear on scaling-range exponents in a turbulent jet. *Phys. Rev.* E **64** (2), 026302.

https://doi.org/10.1017/jfm.2021.399 Published online by Cambridge University Press

MYDLARSKI, L. & WARHAFT, Z. 1996 On the onset of high-Reynolds-number grid-generated wind tunnel turbulence. *J. Fluid Mech.* **320**, 331–368.

NELKIN, M. 1994 Universality and scaling in fully developed turbulence. *Adv. Phys.* **43** (2), 143–181.

OBUKHOV, A. 1962 Some specific features of atmospheric turbulence. *J. Fluid Mech.* **13** (1), 77–81.

PEARSON, B. & ANTONIA, R. 2001 Reynolds-number dependence of turbulent velocity and pressure increments. *J. Fluid Mech.* **444**, 343–382.

VAN REEUWIJK, M. & HOLZNER, M. 2014 The turbulence boundary of a temporal jet. *J. Fluid Mech.* **739**, 254–275.

SABELNIKOV, V., LIPATNIKOV, A.N., NISHIKI, S. & HASEGAWA, T. 2019 Investigation of the influence of combustion-induced thermal expansion on two-point turbulence statistics using conditioned structure functions. *J. Fluid Mech.* **867**, 45–76.

SADEGHI, H., LAVOIE, P. & POLLARD, A. 2015 Equilibrium similarity solution of the turbulent transport equation along the centreline of a round jet. *J. Fluid Mech.* **772**, 740–755.

SADEGHI, H., OBERLACK, M. & GAUDING, M. 2018 On new scaling laws in a temporally evolving turbulent plane jet using lie symmetry analysis and direct numerical simulation. *J. Fluid Mech.* **854**, 233–260.

SAFFMAN, P. 1967 The large-scale structure of homogeneous turbulence. *J. Fluid Mech.* **27** (3), 581–593.

SCHUMACHER, J., SCHEEL, J.D., KRASNOV, D., DONZIS, D.A., YAKHOT, V. & SREENIVASAN, K.R. 2014 Small-scale universality in fluid turbulence. *Proc. Natl Acad. Sci.* **111** (30), 10961–10965.

DA SILVA, C.B., HUNT, J.C., EAMES, I. & WESTERWEEL, J. 2014 Interfacial layers between regions of different turbulence intensity. *Annu. Rev. Fluid Mech.* **46**, 567–590.

DA SILVA, C.B. & PEREIRA, J.C. 2008 Invariants of the velocity-gradient, rate-of-strain, and rate-of-rotation tensors across the turbulent/nonturbulent interface in jets. *Phys. Fluids* **20** (5), 055101.

DE SILVA, C.M., KRUG, D., LOHSE, D. & MARUSIC, I. 2017 Universality of the energy-containing structures in wall-bounded turbulence. *J. Fluid Mech.* **823**, 498–510.

SILVA, T.S., ZECCHETTO, M. & DA SILVA, C.B. 2018 The scaling of the turbulent/non-turbulent interface at high Reynolds numbers. *J. Fluid Mech.* **843**, 156–179.

SINHUBER, M., BODENSCHATZ, E. & BEWLEY, G.P. 2015 Decay of turbulence at high Reynolds numbers. *Phys. Rev. Lett.* **114** (3), 034501.

SPEZIALE, C.G. & BERNARD, P.S. 1992 The energy decay in self-preserving isotropic turbulence revisited. *J. Fluid Mech.* **241**, 645–667.

SREENIVASAN, K.R. & ANTONIA, R. 1997 The phenomenology of small-scale turbulence. *Annu. Rev. Fluid Mech.* **29** (1), 435–472.

STEPHAN, M. & DOCTER, J. 2015 JUQUEEN: IBM Blue Gene/Qő supercomputer system at the Jülich supercomputing centre. *JLSRF* **1**, 1.

TANG, S., ANTONIA, R., DJENIDI, L., DANAILA, L. & ZHOU, Y. 2017 Finite Reynolds number effect on the scaling range behaviour of turbulent longitudinal velocity structure functions. *J. Fluid Mech.* **820**, 341–369.

TANG, S., ANTONIA, R., DJENIDI, L. & ZHOU, Y. 2016 Complete self-preservation along the axis of a circular cylinder far wake. *J. Fluid Mech.* **786**, 253–274.

THIESSET, F., ANTONIA, R. & DANAILA, L. 2013*a* Restricted scaling range models for turbulent velocity and scalar energy transfers in decaying turbulence. *J. Turbul.* **14** (3), 25–41.

THIESSET, F., ANTONIA, R. & DJENIDI, L. 2014*a* Consequences of self-preservation on the axis of a turbulent round jet. *J. Fluid Mech.* **748**, R2.

THIESSET, F., DANAILA, L. & ANTONIA, R. 2013*b* Dynamical effect of the total strain induced by the coherent motion on local isotropy in a wake. *J. Fluid Mech.* **720**, 393–423.

THIESSET, F., DURET, B., MÉNARD, T., DUMOUCHEL, C., REVEILLON, J. & DEMOULIN, F.X. 2020 Liquid transport in scale space. *J. Fluid Mech.* **886**, A4.

THIESSET, F., SCHAEFFER, V., DJENIDI, L. & ANTONIA, R. 2014*b* On self-preservation and log-similarity in a slightly heated axisymmetric mixing layer. *Phys. Fluids* **26** (7), 075106.

TOWNSEND, A. 1949 The fully developed wake of a circular cylinder. *Aust. J. Chem.* **2** (4), 451–468.

TOWNSEND, A. 1951 On the fine-scale structure of turbulence. *Proc. R. Soc. Lond.* A **208** (1095), 534–542.

WATANABE, T. & GOTOH, T. 2007 Inertial-range intermittency and accuracy of direct numerical simulation for turbulence and passive scalar turbulence. *J. Fluid Mech.* **590**, 117–146.

WATANABE, T., DA SILVA, C. & NAGATA, K. 2020 Scale-by-scale kinetic energy budget near the turbulent/nonturbulent interface. *Phys. Rev. Fluids* **5** (12), 124610.

WATANABE, T., DA SILVA, C.B. & NAGATA, K. 2019 Non-dimensional energy dissipation rate near the turbulent/non-turbulent interfacial layer in free shear flows and shear free turbulence. *J. Fluid Mech.* **875**, 321–344.

WESTERWEEL, J., FUKUSHIMA, C., PEDERSEN, J.M. & HUNT, J. 2009 Momentum and scalar transport at the turbulent/non-turbulent interface of a jet. *J. Fluid Mech.* **631**, 199–230.

https://doi.org/10.1017/jfm.2021.399 Published online by Cambridge University Press

YASUDA, T. & VASSILICOS, J.C. 2018 Spatio-temporal intermittency of the turbulent energy cascade. *J. Fluid Mech.* **853**, 235–252.

ZHOU, Y. & VASSILICOS, J. 2020 Energy cascade at the turbulent/nonturbulent interface. *Phys. Rev. Fluids* **5** (6), 064604.

https://doi.org/10.1017/jfm.2021.399 Published online by Cambridge University Press